# FLUID INCLUSIONS: EVIDENCE FOR A COUNTERCLOCKWISE P-T TRAJECTORY IN THE CENTRAL MAINE TERRANE OF SOUTH-CENTRAL MASSACHUSETTS
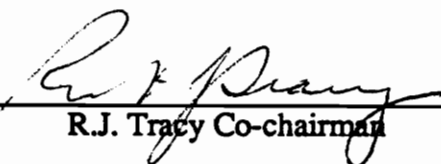
by

David M. Winslow

Thesis submitted to the faculty of the
Virginia Polytechnic Institute and State University
in partial fulfillment of the requirements for the degree of

MASTER OF SCIENCE

in

Geology

APPROVED

_____
R.J. Tracy Co-chairman

_____
R.J. Bodnar Co-chairman

_____
R.D. Law

May, 1991
Blacksburg, Virginia

**Abstract**

Acadian (Late Silurian-Early Devonian) metamorphism in the Central Maine Terrane (CMT) in central Massachusetts is characterized by an early low-P, high-T (Buchan-type) metamorphism followed by compression and nearly isobaric cooling to 100-200°C below peak recorded temperatures before eventual unroofing. Evidence for this path includes sillimanite pseudomorphs after early andalusite, abundant cordierite in pelitic lithologies, late replacement of low-P cordierite-bearing assemblages by high-P garnet-bearing assemblages, recrystallization of mylonites associated with late shear zones to form lower-T and higher-P assemblages, and development of high density $CO_2$ inclusions in the host rock of the mylonite. Peak conditions in the highest grade rocks were 685 - 780°C and 5-6 kbar; the cooling path passed through 550°C at pressures of 6.5-8 kbar.

Fluid inclusion data show a range of fluid composition and density during metamorphism. Densities of $CO_2$ fluid inclusions range from 0.25 g·cm$^{-3}$ to 1.04 g·cm$^{-3}$. High density fluid inclusions are contained within quartz inclusions in garnets found in partial melt leucosomes, and in quartz grains within migmatites. Fluid inclusions within the quartz inclusions indicate trapping conditions of 650-700°C at pressures below 5 kbar. Other $CO_2$ fluid inclusions from matrix quartz yield isochores which pass through conditions of 700°C and 5.2 kbar. The higher density inclusions associated with rocks containing the late high-P assemblages have isochores which pass through the estimated P-T conditions for the recrystallization of the mylonite.

Fluid inclusions recording late stage conditions include $CO_2$-rich, $N_2$-rich and aqueous fluid inclusions. Cathodoluminescence maps of quartz along healed microfractures are used to constrain the late stages of the uplift path.

Fluid inclusion evidence suggests an early isobaric heating event followed by cooling and compression with a later isothermal decompression. This evidence is in

accordance with previously obtained petrologic evidence and supports a counterclockwise

P-T model for the CMT of south-central Massachusetts.

# ACKNOWLEDGEMENTS

I owe the out come of my education at VPI&SU to several individuals whom have contributed greatly to my intellect and my ability to persevere.  First I would like to express my gratitude to my mother who instilled in me a respect for knowledge to the point where learning was fun and not a chore. I owe much gratitude to my soon to be wife Victoria from whom I learned the meaning of the word love.  She was always there to give me encouragement when I thought my work was not up to par or was depressed for any number of other assorted reasons.

My academic success (if success we can call it) is due mainly to the patience and teachings of two men, Dr. Robert Tracy and Dr. Robert Bodnar.  Both were very patient in trying to improve my writing techniques and I apologize for the amount of red pens they have gone through editing my various papers (I promise to replace them).  Probably one of the most important lessons I learned was how to conduct successful research and I hope to carry this on with me in my future career.

Aside from my official advisors I had many fellow graduate students and friends from whom I've learned a lot and often went to with questions. Petrology questions were patiently and willingly explained to me by Matt Nyman and Tom Armstrong, both of whom will be working for me as field assistants in the Himalayas of western Pakistan (woof!).  I owe much of my understanding of my interpretations to them.  Fluid inclusion questions were addressed to Ron Sheets who always answered my question with a question (when he wasn't mumbling).  Also, Charlie Oakes usually had valuable input to any questions I might have had.  I would like to thank Cheryl Erickson and Jeff Seitz for their help with Raman analyses of my fluid inclusions.

Then there is John Mavrogenes (pops).  John made a valiant effort to try to

# TABLE OF CONTENTS

# LIST OF FIGURES

# LIST OF TABLES

# INTRODUCTION

This study was undertaken in order to provide an independent test of a petrologic model for a counterclockwise P-T trajectory in the Central-Maine Terrane (CMT) of south-central Massachusetts (Tracy and Robinson, 1980) through the use of fluid inclusion techniques. Fluid inclusions from several other metamorphic belts have been used in conjunction with petrologic techniques to constrain cooling-unroofing P-T pathways (Hollister *et al.*, 1979; Stout *et al.*, 1986; Hames *et al*, 1989). Although fluid inclusions alone cannot provide an unambiguous model for uplift of a metamorphic terrane, combining these data with data obtained from other petrologic techniques can provide meaningful insight into P-T paths.

The CMT of south-central Massachusetts shows petrologic evidence for an early-stage low-P and high-T (Buchan-type) metamorphism succeeded by loading and cooling to 100-200 degrees Celsius below peak temperatures. Evidence includes probable sillimanite pseudomorphs after andalusite, abundant cordierite in pelitic lithologies, and late replacement of some low-P cordierite-bearing assemblages with high-P garnet-bearing assemblages. Peak metamorphic conditions recorded near Sturbridge, Massachusetts, were 730-780°C at 5.6-6.3 kbar (Robinson *et al.*, 1989); the cooling and unroofing path appears to have passed through 550°C at pressures of 6.5-8 kbar before decompression began (Tracy and Dietsch, 1982). Garnet-biotite and garnet-cordierite geothermobarometry of late stage mylonites which crosscut previous fabrics and which contain the assemblage garnet, cordierite, sillimanite, biotite, K-feldspar and quartz yields pressures of 7-8 kbar at a temperature of 550°C. This counterclockwise P-T path is the reverse of typically modeled decompression-heating paths (e,g., England and Richardson, 1977). Due to the unusual nature of the apparent metamorphic path of these rocks it was desirable to obtain

independent fluid inclusion data to corroborate the petrologic conclusions and to provide further constraints on the cooling path.

Fluid inclusion data were obtained from 8 sample areas representing different lithologies across the CMT. The data show that a range of variable-density fluid inclusions were trapped over a period of time. The relative timing of entrapment was deduced through petrology and crosscutting relationships. Among the different fluid inclusions found were: fluid inclusions trapped within quartz inclusions in garnets found in partial melt leucosomes and a few found in the host rocks associated with the late stage mylonitization. In addition to these inclusions, numerous planes of late stage aqueous fluid inclusions which are useful in determining the lower P-T section of the uplift path, were observed.

## GEOLOGIC AND PETROLOGIC BACKGROUND

The south-central Massachusetts Acadian metamorphic high occupies an area east of the gneiss domes of the Bronson Hill Belt in the center of the CMT. The study area is bounded on the south by the Connecticut border and on the north by the Quabbin Reservoir (Figure 1). The Bronson Hill Belt, the western boundary of the area sampled, is a north-northeast trending belt of gneiss domes thought to involve volcanic and plutonic rocks related to a Taconian island arc terrane (Robinson and Hall, 1980; Hatch *et al.*, 1984, Tucker and Robinson, 1990). The belt runs south to the Long Island Sound and north into Maine. Immediately to the east of the Bronson Hill Belt lies the CMT which contains some of the highest grade metamorphic rocks in New England.
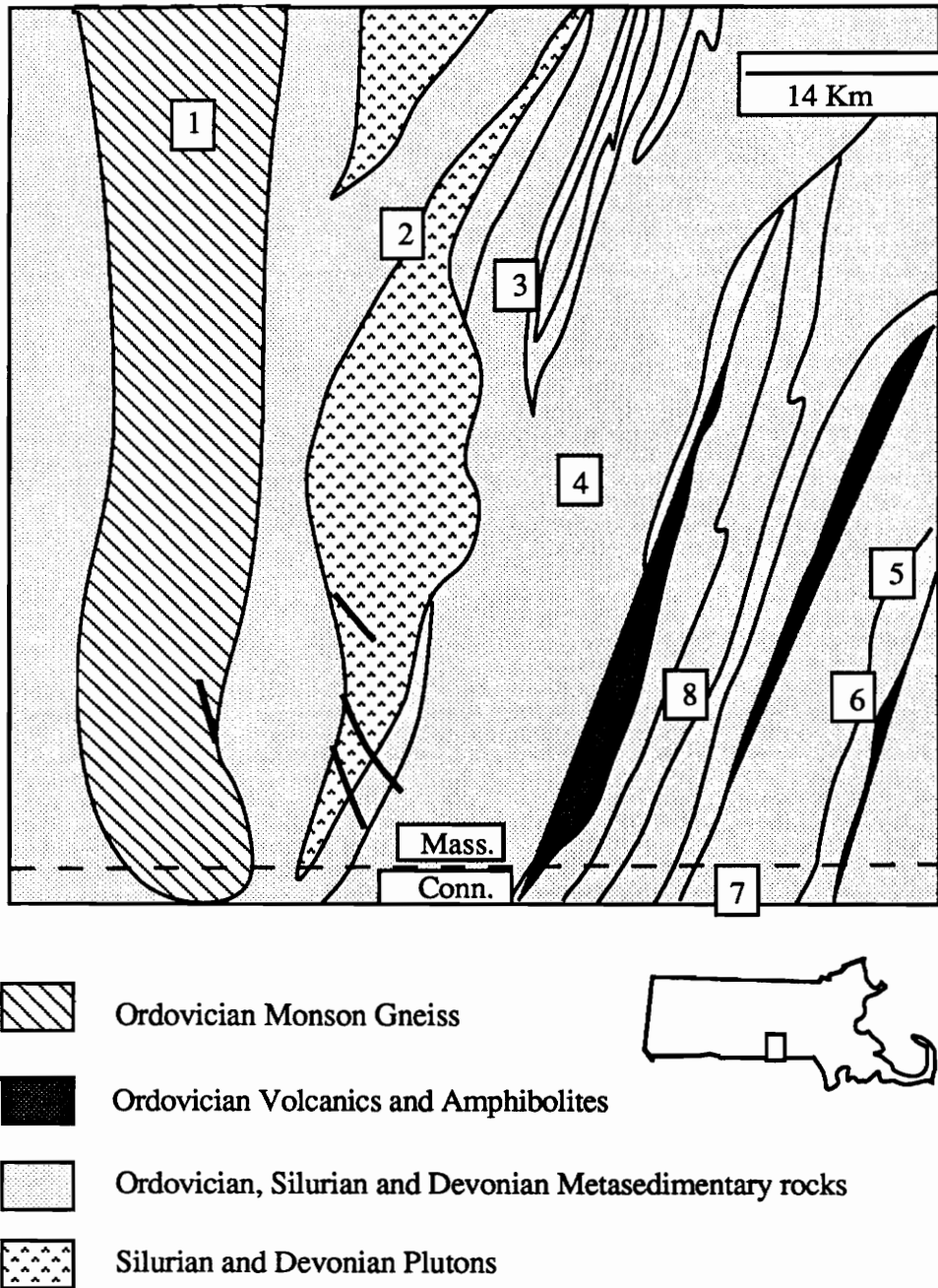
Figure 1. Schematic geologic map of south-central Massachusetts. The numbers refer to sample locations corresponding to Table 1. (modified after Robinson *et al.*, 1989)

## Tectonic-Metamorphic Model

The Bronson Hill Belt and CMT show very complex deformational behavior which has been synthesized into a regional tectonic model (Robinson *et al.*, 1989). In this model, three deformation stages are reflected in the structures and metamorphism of the area.

Stage one consisted of regional scale emplacement of west-vergent fold and thrust nappes. Contemporaneous with this event was the intrusion of calc-alkaline plutons ranging in composition from gabbros through biotite tonalites and granites. Toward the east, probably high up in the original nappe pile, there is evidence for a low pressure, high temperature metamorphic event. This evidence includes occurrences of rocks containing probable andalusite preserved in pseudomorphs and at least one relict contact aureole adjacent to an augite-horneblende diorite which suggests that there was early plutonic activity (Shearer and Robinson, 1980).

In stage two, the axial surfaces of the earlier west directed nappes were backfolded on a large scale into recumbent folds and nappes overturned to the east. Peak metamorphism predated the early backfold stage but occurred after the west-directed thrust nappes, and resulted in abundant sillimanite, K-feldspar, garnet, cordierite assemblages at temperatures of 685-780°C and pressures of 5.6-6.3 kbar. At many locations peak metamorphic mineral lineations are cut by ductile mylonites assigned to the backfold stage of deformation (Robinson *et al.*, 1989). The backfold stage is part of a continuum with the dome stage deformation, with mylonite development occurring at the end of the backfold stage.

Timing of Acadian metamorphism and associated deformation is constrained by the involvement of lower Devonian strata. Recent dating by Sm/Nd and U/Pb techniques has produced ages of 420-405 Ma for Silurian-Devonian plutons (Barriero and Aleinikoff, 1985; Moench and Aleinikoff, 1991). The Beltchertown pluton truncates folds of the

earlier deformations and has an unmetamorphosed pyroxene-rich core which yields Pb/Pb zircon ages of 380 Ma (Ashwal *et al.*, 1979). A better constraint on the end of Acadian peak metamorphism and nappe stage deformation is a 408 Ma age using U/Pb on zircon in a post metamorphic quartz-graphite vein from Bristol, New Hampshire (Zeitler *et al.*, 1990).

## Petrology

Sedimentary and volcanic rock units of the CMT range from Lower Ordovician to Lower Devonian in age and are thought to represent an extensive backarc sedimentary basin active between the Middle Ordovician and Late Silurian (Moench and Aleinikoff, 1991; Tracy, *et al.*, 1991; Armstrong *et al.*, in review). Units sampled from within the CMT include the Rangeley Formation (Silurian), Paxton Formation (Silurian), and the Littleton Formation (Devonian) as well as one pluton, the Coys Hill granite. These units have been dated by along-strike correlations in western Maine and New Hampshire (Hatch *et al.*, 1983). Metasedimentary rocks from the CMT have been intruded by early Devonian tonalites and granites as well as by minor gabbro and diorite. The eastern part of the belt comprises units lithologically similar to those in the west, but granitic to intermediate intrusions of Ordovician, Silurian and Devonian ages are present.

Pelitic gneisses of the CMT contain the assemblage quartz (qtz)-biotite (bio)-plagioclase (pl)-K-feldspar (Kfs)-cordierite (crd)-sillimanite (sil)-garnet (gar) $\pm$ pyrrhotite (po) $\pm$ pyrite (py) $\pm$ graphite (gr) $\pm$ ilmenite (ilm) $\pm$ rutile (rt) (Table 1 and Figure 2). In addition to the common pelitic gneisses many rocks contain local partial melting, pegmatitic intrusions and calc-silicate pods. Garnets typically occur as porphyroblasts and locally contain sillimanite, quartz and biotite inclusions.

Migmatites and felsic intrusions showing evidence for an earlier fluid present melting (Robinson *et al.*, 1989; Thompson *et al.*, 1968) are common in the high grade

Table 1. Mineral assemblages and fluid inclusions in eight samples examined
in the study.  Sample locations 1-8 correspond to locations shown on Figure
1.

| Sample Location | Sample # | Assemblage | Fluid inclusions |
| --- | --- | --- | --- |
| 1 | WD-1 | qtz, pl, gar, hbl, bio, Kfs, sil | $CO_2$-$N_2$ |
| 2 | CH-1 | qtz, Kfs, pl sil, bio, gar | $H_2O$-NaCl and $CO_2$ |
| 3 | WN-5 | qtz, pl, Kfs, bio, gar, crd, sil | $N_2$ and $CO_2$ |
| 4 | WN-7 | crd, gar, qtz, pl, bio, sil, Kfs, | $CO_2$ and $N_2$ |
| 5 | 76228 | pl, qtz, Kfs, gar, sil | $CO_2$ and $H_2O$-NaCl |
| 6 | SB-10 | bio, Kfs, gar, crd, sil, pl, qtz | $CO_2$ |
| 7 | WN-9 | qtz, Kfs,pl, bio, cpx, opx, hbl, sil | $CO_2$ |
| 8 | PL-1 | qtz, pl, Kfs, bio, gar, crd, sil | $N_2$ |
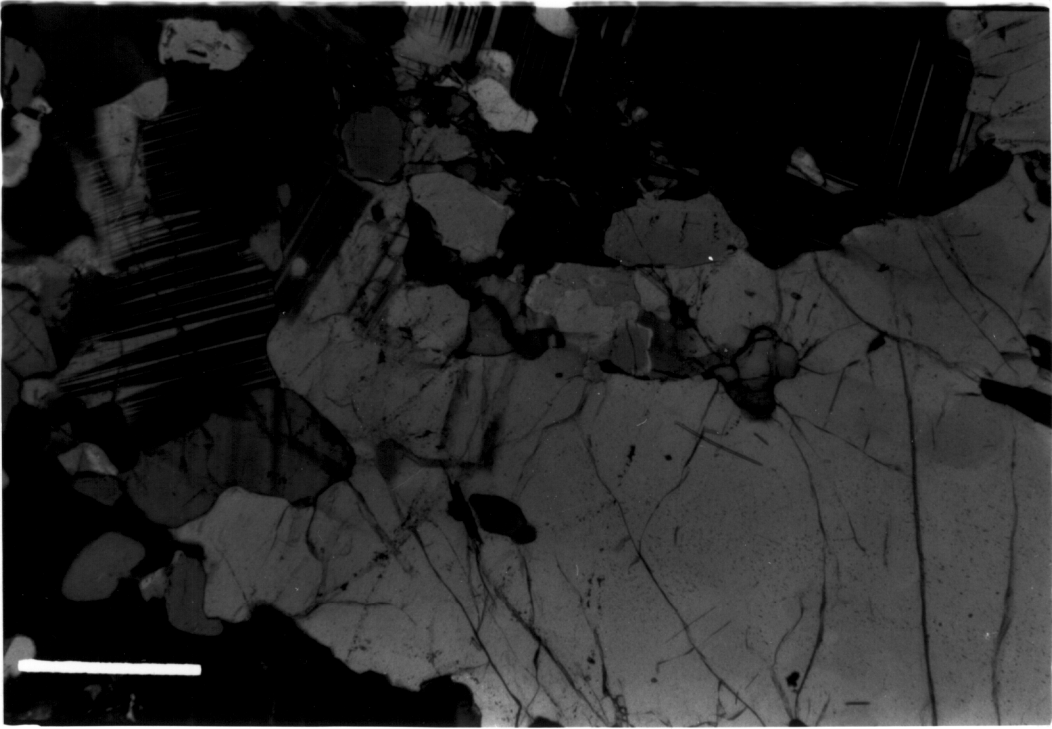
Figure 2.    Photomicrograph of sample WN-7, a typical gar-crd-sil-Kfs gneiss of the
CMT.  Scale bar = 240 μm.

rocks of the area.  Leucosomes of partial melts contain the assemblage qtz-pl-Kfs, as well as local occurrences of bio-gar-crd and sil.

One of the sample localities near Sturbridge is a grey-weathering aluminous schist with calc-silicate lenses which have been tentatively assigned to the Rangeley Formation (Robinson *et al.*, 1989).  The rock contains coarse-grained qtz-Kfs-pl-gar-crd-bio-sil and gr.  Also present are two large sill-like pegmatites consisting of gar-retrograde bio-pl-Kfs -qtz and zones of sil-bearing and sil-absent layers.  Surrounding the partial melts are mafic restites consisting of gar-bio-crd and sil.  Partial melting occurred early in the tectonic/metamorphic sequence as suggested by outcrop relationships (Thompson *et al.*, 1968).

Numerous recrystallized mylonites thought to have formed at the end of the backfold stage of deformation (Figure 3) are present within the Rangeley Formation. These mylonites are of particular importance in determination of the proposed P-T trajectory because they crosscut all previous mineral lineations and dome stage folds are preserved within them (Robinson *et al.*, 1989).  The mylonites probably represent conditions prevalent during the later stages of metamorphism.  The mylonite considered here is from sample WN-7 and has been studied in great detail by Robinson *et al.,* (1989).

In the present study the mylonite was examined and compared with the granulite host rock.  The host rock assemblage is bio-pl-crd-gar-Kfs and sil with po and apatite as accessory minerals.  Within the mylonite, biotite is the most abundant mineral but decreases in abundance away from the mylonitic band.  Outside the band biotite occurs as scattered patches.  Grain size in the host rock abruptly coarsens at the contact with the mylonite reaching a maximum grain size of 1.6 mm in the host rock.

Figure 3.    Photomicrograph of the late stage mylonite from sample WN-7.  Scale bar = 480 μm.

The mylonite zone contains the assemblage gar-bio-sil-Kfs and qtz with clasts of crd and Kfs. Garnets growing in the mylonite do not quite achieve euhedral crystal form. Definite euhedral qualities can be seen in some of the garnets (Figure 4), while others appear skeletal, thereby destroying the euhedral nature of the minerals. The poikiloblastic nature of the garnets as well as some oriented inclusions show that they grew during or after recrystallization of the mylonite (Robinson *et al.*, 1989). Relict garnets would show signs of the mylonite foliation wrapping around the clasts. The cordierite seems to be from an assemblage produced before the growth of the garnets. Whereas the garnets crosscut the foliation cordierite occurs as rotated clasts within the mylonite.

## ANALYTICAL PROCEDURES

### Fluid Inclusion Techniques

Fluid inclusion composition and density were determined by standard heating and freezing measurements on a Fluid INC. adapted USGS gas flow heating and freezing stage. While determining temperatures of phase changes a heating rate of 1°C/ minute was used so as to increase the accuracy of measurements by allowing time to document the phase changes. The heating and freezing stage was calibrated at three temperatures, the critical point of water (374°C), the freezing point of pure water (0°C) and the triple point of carbon dioxide (-56.6°C), using synthetic fluid inclusions. Measured temperatures have precision of $\pm 0.1$°C at temperatures $\leq 50$°C, and $\pm 2.5$°C at temperatures around 375°C. Densities of saline solutions were calculated using the PVT properties of $H_2O$-NaCl (Bodnar, 1985). Salinities of aqueous inclusions were determined from freezing point depressions of $H_2O$ and the eutectic temperature (first melting of ice) of the solution (Hall *et al.*, 1988). Fluid inclusion isochores were calculated with the PVT data of Bodnar (1985) for aqueous inclusions and using the modified Redlich-Kwong equation of state of

Figure 4.    Photomicrograph from the late stage mylonite of sample WN-7 showing a late stage garnets. Note the euhedral nature of the garnet.
Scale bar = 28 μm.

Holloway (1981) corrected to make the *a* term temperature dependent for $CO_2$. Temperatures of phase changes were recorded during heating runs to avoid nucleation problems.

Paragenesis of late stage fluid inclusion planes was defined using cathodoluminescence (CL) maps constructed using the CL mode of the Cameca SX 50 electron microprobe at operating conditions of 40 Kv and 165 nanoamp beam current. The advantage of using this technique compared to conventional petrologic techniques to determine fluid inclusion paragenesis is that the luminescent properties of the quartz enhance our ability to determine cross cutting relationships.

**Petrologic Techniques**

All electron microprobe analyses were done on polished thin sections using a Cameca SX 50 fully automated electron microprobe. Operating conditions were 15 kv accelerating potential and 20 nanoamps beam current for the cordierites and garnets. The biotites required a 15 kv accelerating potential with a 10 nanoamp beam current. Probe data were reduced using a ZAF correction (Heinrich, 1981). Mineral formula calculations were based on the method of Deer *et al.* (1976).

Analytical schemes were set up to analyze garnet, cordierite, and biotite and measured mineral compositions were used to determine partition coefficients for the appropriate exchange reactions which were then used to determine pressures or temperatures of equilibration using calibrated mineral exchange thermobarometers. The garnet-biotite calibration of Ferry and Spear (1978) was combined with the almandine activity model of Hodges and Crowley (1985) to determine equilibration temperatures using garnet-biotite thermometry. Pressures were determined using the garnet-cordierite barometer with the calibrations of Thompson (1976) and Holdaway and Lee (1977).

## RESULTS

### Mineral Chemistry

Biotite. Analyses were obtained on biotites from granulite facies sil-bio-gar-crd gneisses as well as from associated late stage mylonites. A theoretically determined 3.8-4.0 wt % water was added to the analyses in order to account for the water in the biotite structure. When this was done, oxide totals approached 100%. Structural formulas were calculated on the bases of 22 oxygens on the assumption that $Si^{IV}$ and $Al^{IV}$ filled all the tetrahedral sites. Any remaining Al is assumed to go into the octahedral sites.

Biotite composition was found to vary between the mylonite and the undeformed rock with Fe/(Fe+Mg) dropping off in the mylonite from 0.39 to 0.33 (Table 2). This increase in Mg and decrease in Fe is also associated with a decrease in Ti content within the mylonite. Biotites from the mylonite typically have Ti concentrations of 1.9-2.2 wt % while biotites in the host rock show contents of 2.7 wt %. Previous studies have shown that Ti increases as temperature and pressure increase (Guidotti, 1984).

Within the mylonite some larger biotites also preserve zonation of Fe and Mg. Biotite cores contain Fe/(Fe + Mg) of .37 $\pm$ .01 while at the rims the ratio decreases to .29-.33. This is due to an Fe decrease from core to rim and Mg increase towards the rim. Smaller matrix biotites show no zoning and are compositionally similar to the rims of the larger biotites.

Garnet. Table 2 presents microprobe analyses and structural formulas of garnets from both the mylonite. Garnets from the host rock appear as large porphyroblasts filled with inclusions of biotite, sillimanite and quartz. Garnets in the mylonite occur as small skeletal or euhedral porphyroblasts. In many cases mylonite garnets contain quartz and apatite inclusions which show the foliation of the mylonite (Robinson et al., 1989).

Table 2. Electron microprobe data of representative minerals from sample WN-7. Analyses of biotites and garnets show core and rim compositions within the mylonite. Cordierite analyses show compositions from the mylonite and the host rock. Formula units based on 22 oxygens for biotite, 24 oxygens for garnet and 18 oxygens for cordierites.

| | Garnet core | Garnet rim | Biotite core | Biotite rim | Cordierite host | Cordierite myl. |
|---|---|---|---|---|---|---|
| $SiO_2$ | 39.39 | 38.92 | 37.16 | 33.93 | 47.42 | 47.77 |
| $TiO_2$ | 0.00 | 0.01 | 2.27 | 1.13 | 0.00 | 0.00 |
| $Al_2O_3$ | 23.76 | 23.76 | 20.80 | 21.85 | 32.21 | 32.28 |
| $Cr_2O_3$ | 0.00 | 0.00 | 0.14 | 0.05 | 0.00 | 0.00 |
| MgO | 7.05 | 5.42 | 14.84 | 16.12 | 9.54 | 9.75 |
| CaO | 1.06 | 0.96 | 0.10 | 0.014 | 0.00 | 0.00 |
| MnO | 0.87 | 0.81 | 0.12 | 0.00 | 0.07 | 0.10 |
| FeO | 29.77 | 31.95 | 13.10 | 11.72 | 6.38 | 5.62 |
| BaO | 0.00 | 0.00 | 0.00 | 0.00 | 0.00 | 0.00 |
| $Na_2O$ | 0.00 | 0.00 | 0.30 | 0.09 | 0.16 | 0.09 |
| $K_2O$ | 0.00 | 0.00 | 8.09 | 8.97 | 0.00 | 0.00 |
| $H_2O$ | 0.00 | 0.00 | 3.74 | 3.95 | 0.00 | 0.00 |
| F | 0.00 | 0.00 | 0.94 | 0.42 | 0.00 | 0.00 |
| total | 100.62 | 101.83 | 101.25 | 100.17 | 95.77 | 95.60 |
| | | | | | | |
| cat Si | 6.07 | 5.97 | 5.32 | 5.20 | 4.98 | 5.00 |
| cat Ti | 0.00 | 0.00 | 0.24 | 0.12 | 0.00 | 0.00 |
| cat Al | 4.08 | 4.23 | 3.51 | 3.73 | 3.98 | 3.98 |
| cat Cr | 0.00 | 0.00 | 0.01 | 0.01 | 0.00 | 0.00 |
| cat Mg | 1.62 | 1.24 | 3.17 | 3.47 | 1.49 | 1.52 |
| cat Ca | 0.17 | 0.16 | 0.01 | 0.02 | 0.00 | 0.00 |
| cat Mn | 0.11 | .11 | 0.01 | 0.00 | 0.01 | 0.02 |
| cat Fe | 3.84 | 4.10 | 1.57 | 1.42 | 0.56 | 0.50 |
| cat Ba | 0.00 | 0.00 | 0.00 | 0.00 | 0.00 | 0.00 |
| cat Na | 0.00 | 0.00 | 0.08 | 0.03 | 0.03 | 0.02 |
| cat K | 0.00 | 0.00 | 1.148 | 1.66 | 0.00 | 0.00 |
| total cations | 15.89 | 15.88 | 15.44 | 15.65 | 11.049 | 11.02 |
| | | | | | | |
| Fe/(Fe + Mg) | 0.71 | 0.78 | 0.33 | 0.29 | 0.27 | 0.24 |

Garnets from the mylonite show a rim of Mg depletion and Fe enrichment with the aid of color enhanced X-ray image maps. Detailed traverses of the garnet reveal a drop of Mg at the edge of the garnet as well as an increase in Fe away from the garnet core. Probe traverses across a large garnet porphyroblast from the host rock showed no signs of zoning but reveal a rim of Mg depletion and Fe enrichment (Figures 5 and 6).

Cordierite. Cordierite was found in the host rock and as clasts within the mylonite zone. Cordierites from the host rock are lower in Mg and enriched in Fe relative to those from the mylonite (Table 2). This agrees with a change in mineral composition from the host rock to the mylonite, with the mylonite minerals being enriched in Mg and depleted in Fe. Additionally, X-ray maps show a retrograde depletion in Mg and slight enrichment of Fe along the rims of cordierites from both areas (Figure 7), which probably reflects changing conditions and Fe-Mg reactions with biotite and garnet.

## Singular Value Decomposition

Singular value decomposition (SVD) modelling was used to test whether the observed differences in mineral compositions in the mylonites as compared with the host rock were a result of bulk composition differences or were produced through chemical reactions. In multicomponent assemblages these problems can be solved by investigating the rank, composition space and reaction space of a matrix representing the compositions of the phases involved (Fisher, 1989).

A standard AFM diagram projected through K-feldspar (Figure 8) shows the intersection of the two assemblages. The two assemblages can intersect in AFM space if a
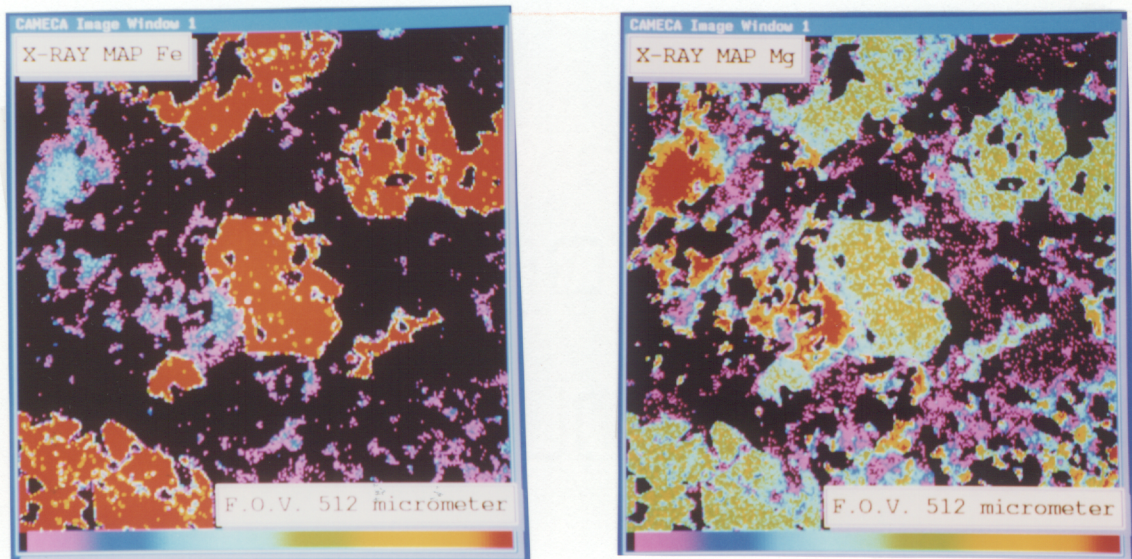
Figure 5    Fe and Mg X-ray maps for garnet and biotite from the late stage mylonite.
The Fe map shows the Fe zoning in the biotites (upper left)
While the Mg map shows the Mg zoning in the garnets (Mg depletion towards
the rim).  The garnets also exhibit Fe zoning with  Fe enrichment towards the
rim.  The biotites show  Fe depletion towards the rim and Mg enrichment
towards the rim.
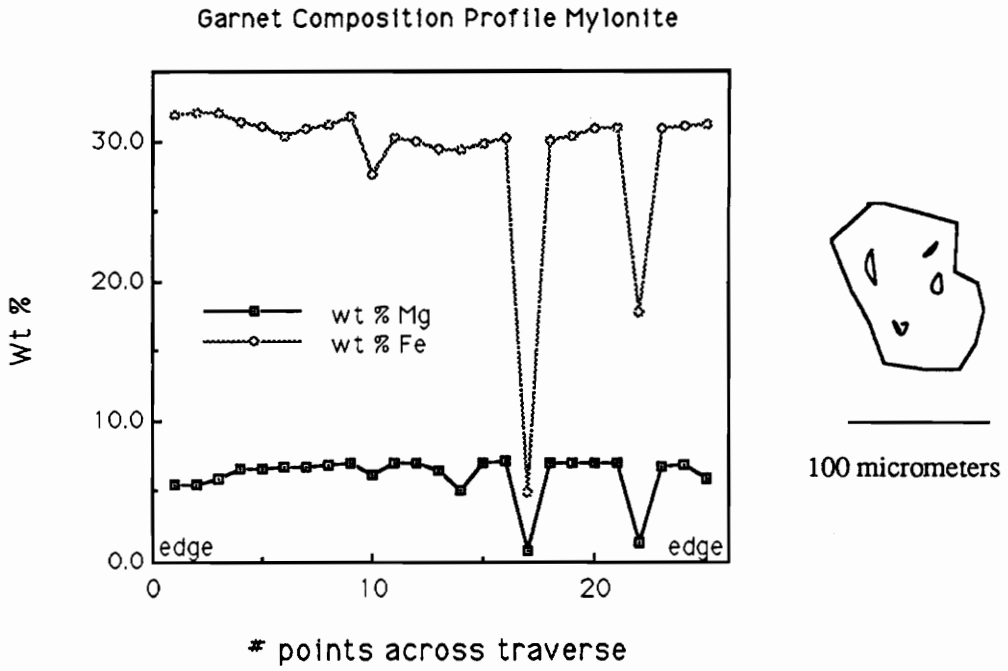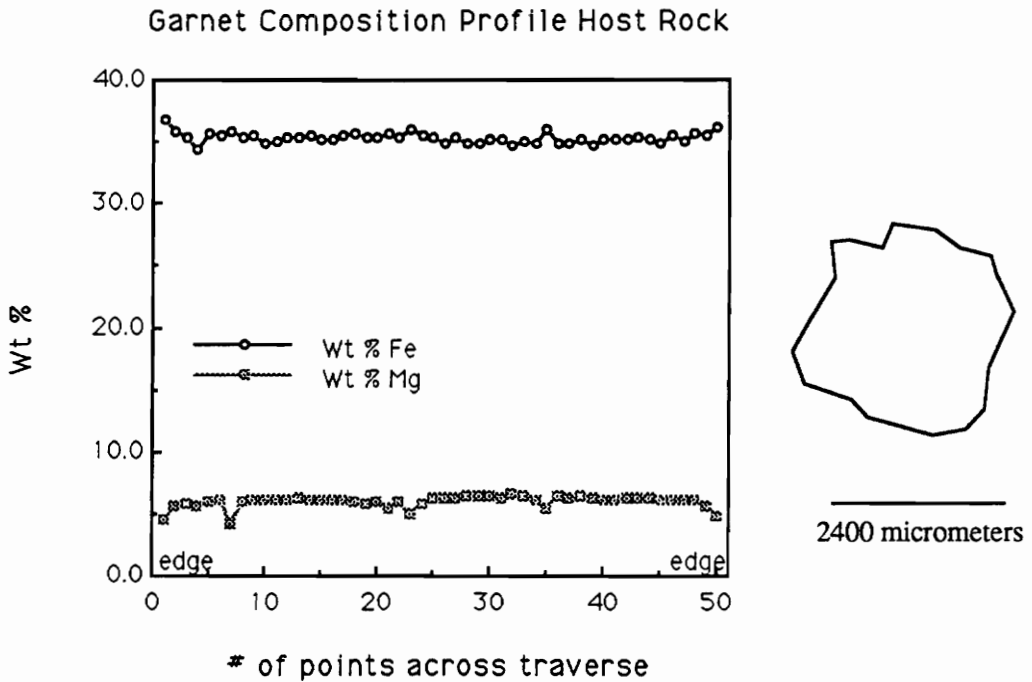
Figure 6. A) Composition profile of garnet within mylonite from sample WN-7. Notice the increase in Fe away from the core. B) Composition profile of garnet from the host rock. Notice the homogeneous nature of the garnet with slight retrograde reequilibration. The spikes across the traverse represent quartz inclusions.
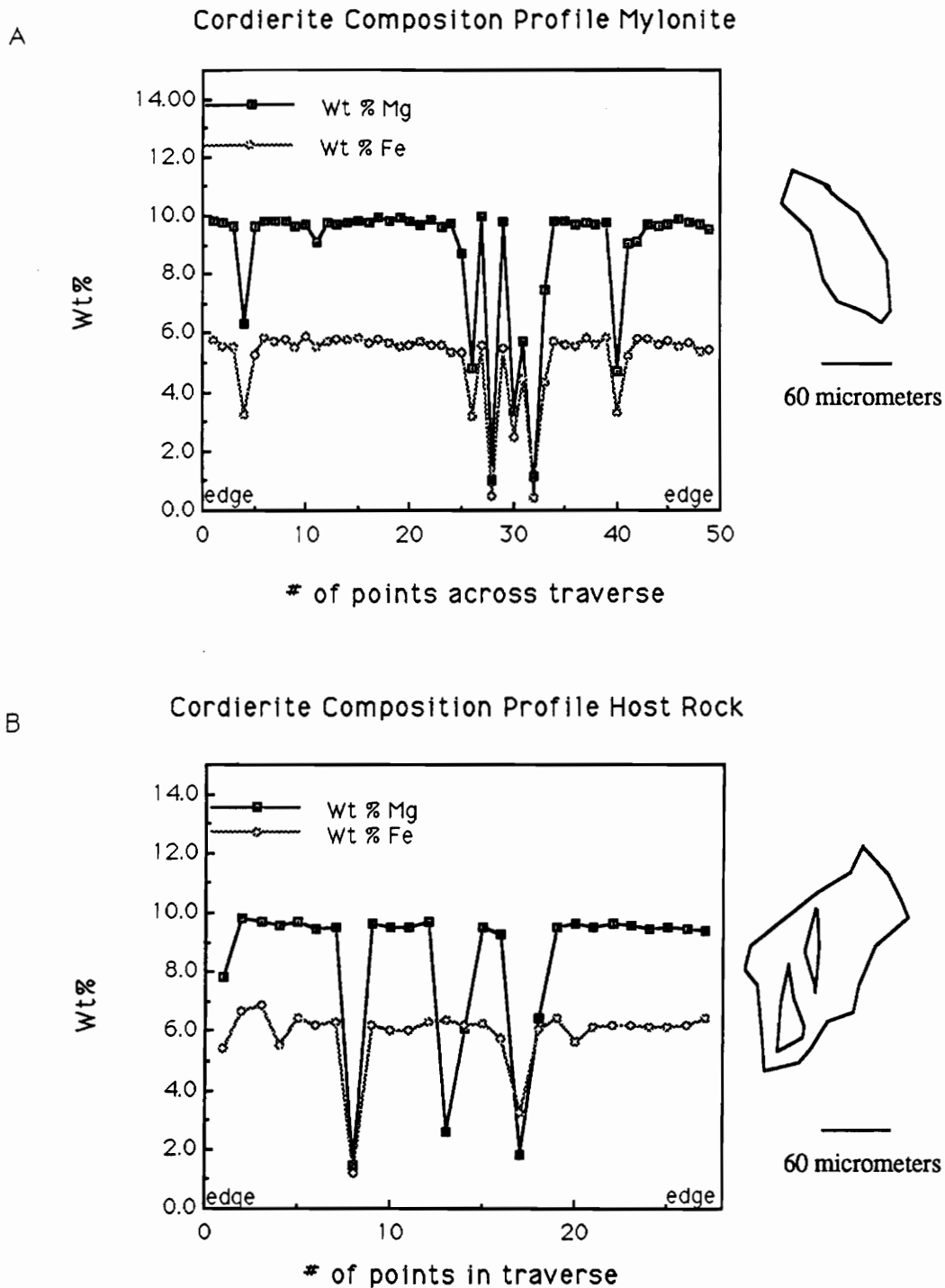
Figure 7  A) Composition profile of cordierite within mylonite from sample WN-7.
Note the relatively homogeneous nature of the mineral with Mg compositions
close to 10 wt % and Fe compostions under 6 wt %  B) Composition profile of
cordierite in the host rock.  Note that Mg compositions are a little lower and Fe
compositions are higher in the mylonite.  Spikes in the traverses represent quartz
inclusions.

K-Feldspar Projection
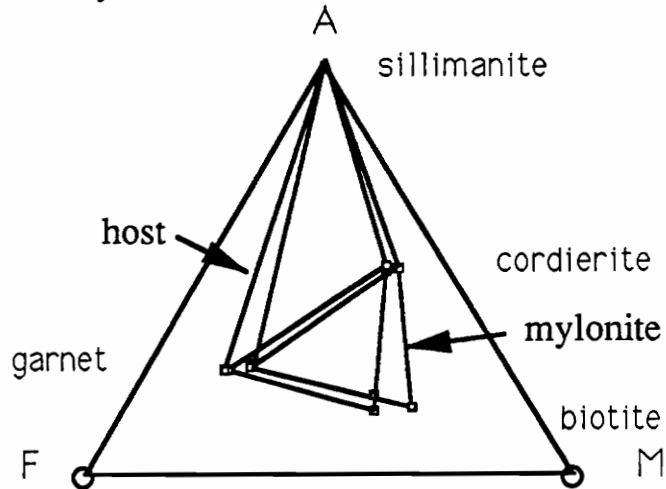


Figure 8   AFM diagram showing the differences in Fe/Fe + Mg
           composition between the mylonite and its host rock.
           Within the mylonite the garnet, biotite and cordierite
           all have a lower Fe/(Fe + Mg) ratio.  This results in
           crossing tie lines which indicate either different
           equilibration conditions or a bulk composition
           overlap.

given bulk composition produces two different equilibrium assemblages under different P-T conditions, or if the bulk compositions of the two assemblages are different. If the intersecting assemblages have any univariant incompatible reactions in which the minerals of one assemblage are reactants and the minerals of the other assemblage are products, then the assemblages do intersect in composition space and cannot have equilibrated under the same conditions.

Running a rank 7 model matrix through SVD and the program MULTI (Fisher, 1989) suggested the following univariant incompatible reactions between the two assemblages (minerals which appear on both sides of the reaction must have different compositions and are differentiated by numbers in parentheses).

1          Gar (1) + Bio (1) + Crd (1) + Kfs =

                Qtz + Gar (2)+ Bio (2) + Sil

2          Bio (1) + Crd (1) + Kfs + Pl =

                Qtz + Gar (2) + Bio (2) + Sil

3          Gar (1) + Bio (1) + Crd (1)  =

                Qtz + Gar (2) + Bio (2) + Crd (2) + Sil
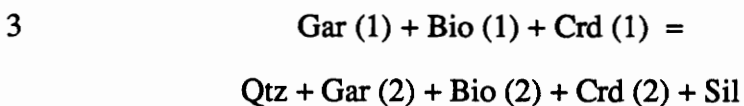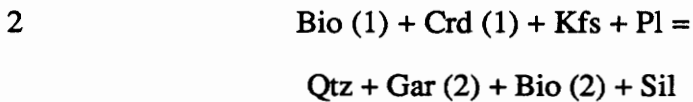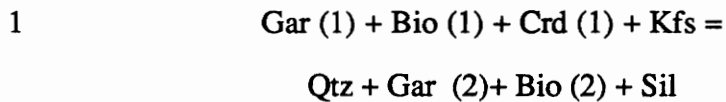
The above reactions were then tested for linear dependencies and none were found, indicating that of the set of components chosen, none could be created through a combination of any others and hence these may be possible reactions

Probably a combination of the above reactions, especially reactions 1 and 2 are responsible for the changes in the assemblages because they agree with what is seen in thin section. The occurrence of these incompatible reactions suggests that the observed changes

in assemblages were a result of mineral reactions responding to different conditions rather then a difference in bulk composition of the two assemblages.

## Fluid Inclusion Microthermometry

Fluid inclusions of varying composition and density were observed throughout the CMT. Fluid inclusion composition ranged from $CO_2$-rich, to $CO_2$-$N_2$-rich, to $N_2$-rich, to aqueous. Within each of these groups several episodes of fluid inclusion entrapment could be determined through microthermometry and petrology.

Type I. $CO_2$-rich Fluid Inclusions. Based on the mode of occurrence, composition and room temperature phase ratios, several distinct types of $CO_2$-rich fluid inclusions were found in samples from across the CMT (Table 1). Because melting temperatures were near -56.6°C and no visible water could be detected within the inclusions, they can be modeled as being pure $CO_2$ (Figure 9). Based on comparison to synthetic fluid inclusions, up to 20 mole % $H_2O$ could be present in the inclusions and not be detected optically [Bodnar, personal communication, 1991]. However, this much $CO_2$ would be revealed from clathrate melting, especially in the larger inclusions. No such behavior has been documented in the analyzed inclusions.

Two modes of occurrence were observed for the $CO_2$ inclusions studied; those which occur along healed microfractures and those which occur as isolated nonplanar arrays of indeterminant origin. The isolated inclusions were found within the partial melt leucosomes of the Littleton Formation and in the Rangeley Formation, where they are associated with the late stage mylonites.

Two populations of $CO_2$ fluid inclusions were defined (Figure 9) based on
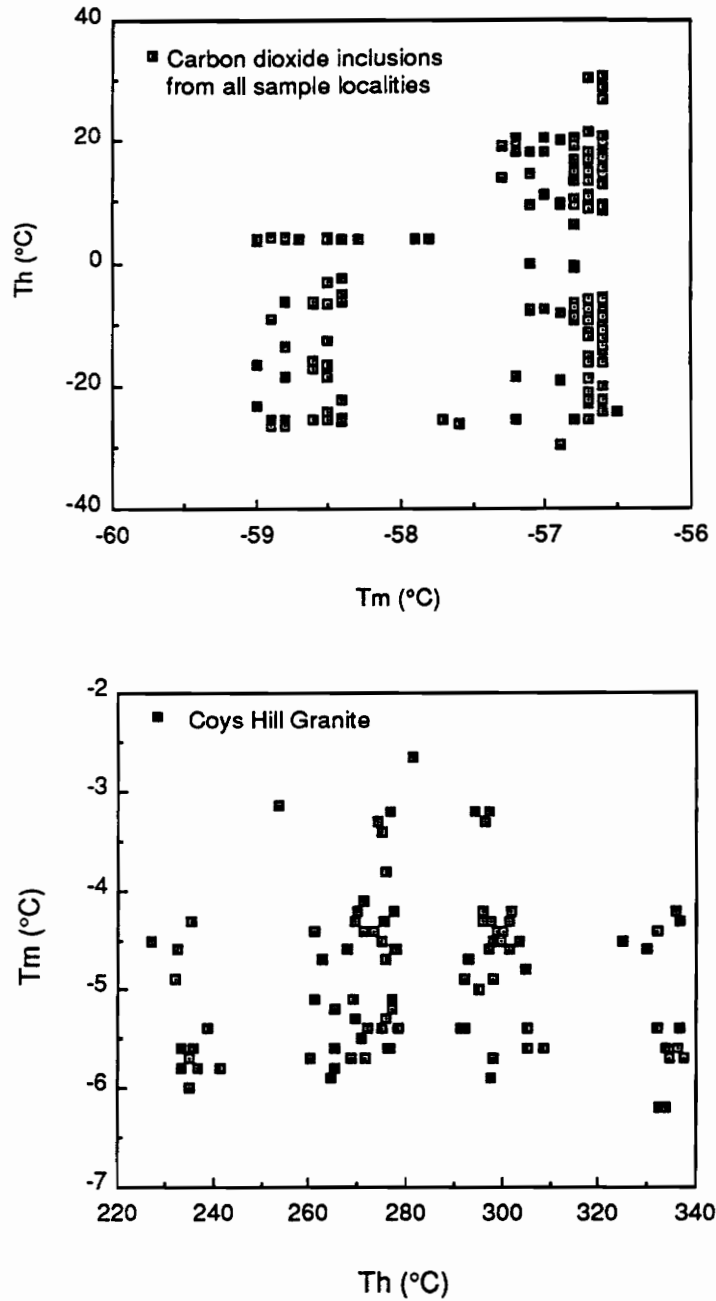
Figure 9.  A) Homogenization temperature [Th(°C)] vs. melting temperature [Tm(°C)] plot for
carbon dioxide rich fluid inclusions.  Notice the two different composition groups as
indicated by melting depressions.  Also note the three groups of different density
inclusions.

B) Homogenization temperature [Th(°C)] vs. melting temperature [Tm(°C)] plot for
aqueous fluid inclusions.  Notice the development of 4 groups of inclusions.  Axes were
switched to emphasize the range of Th.

homogenization temperatures. These include: a group of fluid inclusions with homogenization temperatures in the range of -26 to 0°C, and a group of inclusions with homogenization temperatures between 0 and 30°C. Fluid inclusions with Th of -26 to 0°C contain a subgroup with Th from -26 to -18°C

Fluid inclusions with Th of -26 to -18°C are rare and found only within quartz grains within a few centimeters of the late stage mylonite. At room temperature these inclusions contain a single liquid phase. Upon freezing a solid forms below -100°C and melts over a range of -57 to -56.6°C. During continued heating thermal cycling was used to determine the final homogenization of liquid and vapor due to the small size of the inclusions, < 5 μm.

A second group of inclusions that occur in isolated patches ( Figure 10) homogenizes from -6 to -9°C. At room temperature these inclusions show only a single liquid phase. After freezing the inclusions, melting occurred near -56.6°C. A notable example of these inclusions is found in sample 76228. This sample is a leucogranitic partial melt segregation. Within the segregation are abundant quartz grains, a scattered few contain small groups of $CO_2$-rich fluid inclusions. Fluid inclusions found within this group are generally between 8 and 12 μm in size and show oval to negative crystal shapes.

Amongst the higher Th fluid inclusions are a group found in a quartz inclusion within a garnet xenocryst (Figure 11). Again, at room temperature only a single liquid phase is present in the inclusions. Melting of the $CO_2$ solid occurred between -57.3 and -56.6 °C. Upon further heating homogenization occurred between 8 and 12 °C. These fluid inclusions show negative crystal shape with sizes ranging from 6-12 μm.

The majority of $CO_2$ inclusions analyzed from the higher homogenization
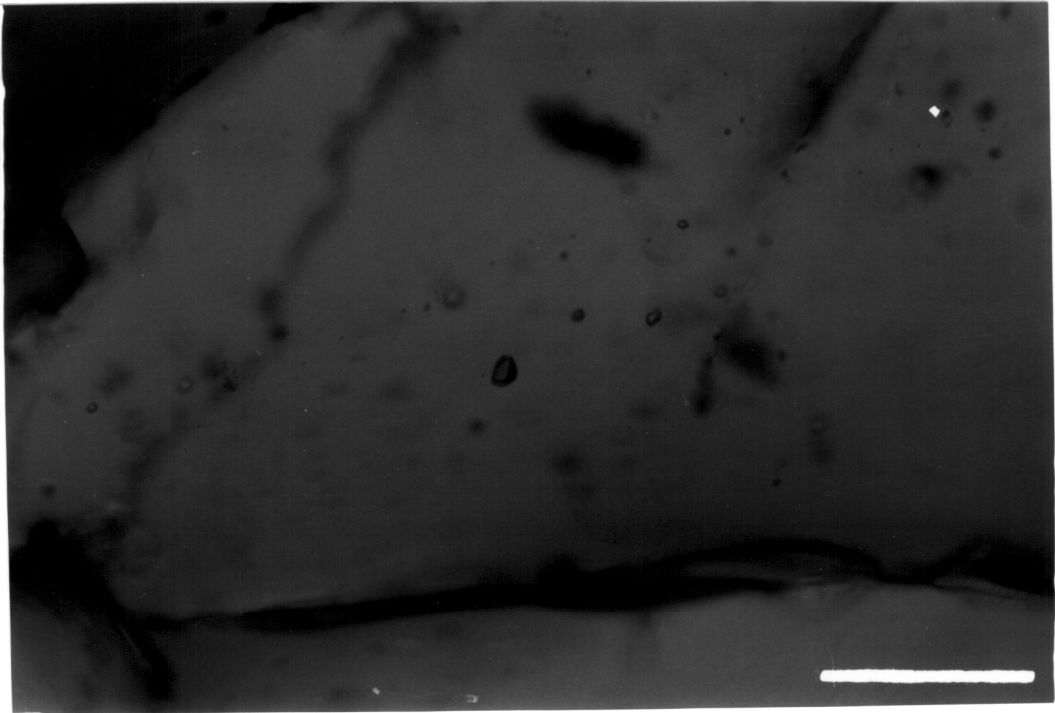
Figure 10.   Fluid inclusions from matrix quartz in granitic leucosome of
             sample76228.
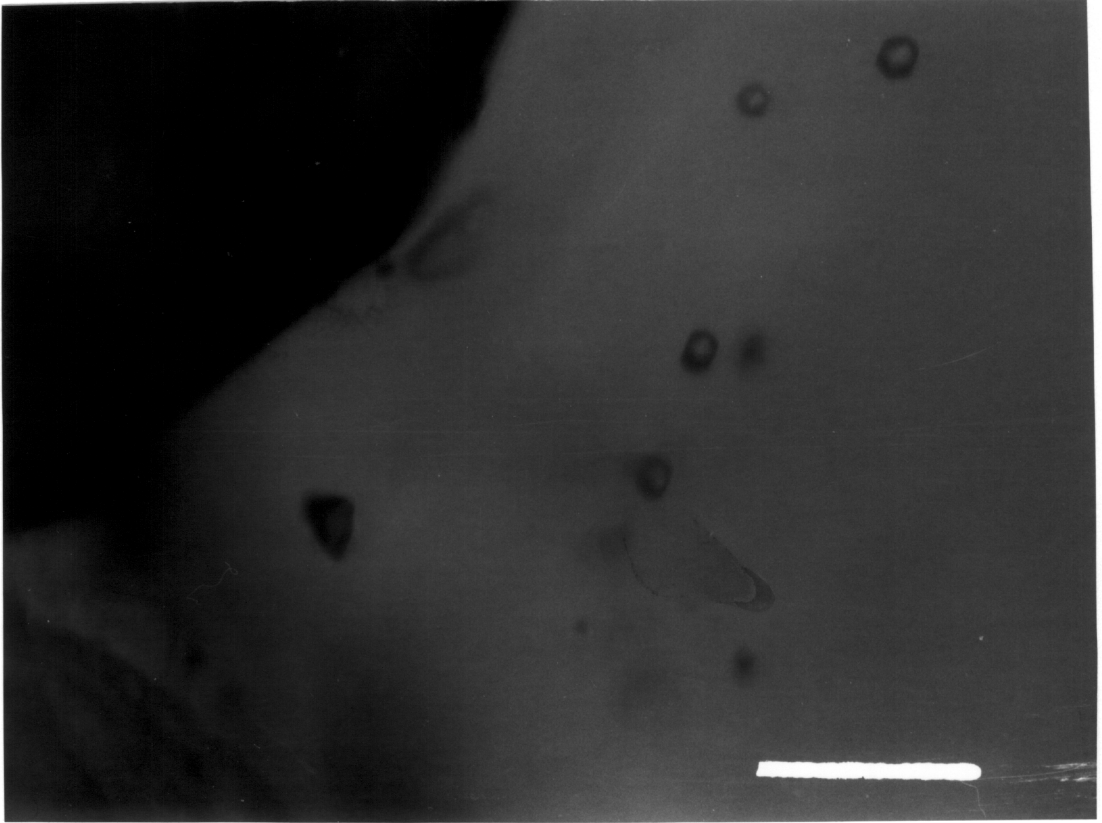
Figure 11.   Fluid inclusions within quartz included within a garnet xenocryst from
sample 76228.  The fluid inclusions are 8-12 μm in size and exhibit  negative
crystal shape.  Scale bar = 28 μm.

temperature group occur along trails, some of which are intergranular. A large proportion of these fluid inclusions exhibit two phases at room temperature. Upon cooling the liquid freezes at < -85°C and melting occurs near -56.6°C. Further heating resulted in homogenization both to the liquid and vapor between 15 and 30 °C.

Type II, $CO_2–N_2$-rich fluid inclusions. A second group of $CO_2$-rich fluid inclusions containing $N_2$ have been documented (Figures 9 and 12) based on laser Raman spectroscopy and freezing point depressions . Sample WD-1A of the Partridge Formation contains abundant $CO_2–N_2$ fluid inclusions. Three different generations of these fluid inclusions can be documented based on microthermometry and morphology. All inclusions show one phase at room temperature. Melting of the solid in these inclusions ranged from -59 to -58°C with homogenization ranging from -25 to 8°C. The first generation consists of scattered, isolated inclusions thought to be of early origin because later planes of inclusions cut through the patches and appear to post date them. Secondary fluid inclusion planes occur throughout the leucosomes and are thought to be formed from fluid derived from decrepitation of earlier trapped fluid inclusions since these inclusions have the same composition but different densities. These trails also cut through some groups of earlier entrapped inclusions. The third generation of inclusions is tubular in shape and found along twin lamellae in plagioclase Fluid inclusion size ranged from 2-20 μm although inclusions found in the plagioclase lamellae were generally larger, < 30 μm.

Type III, $N_2$-rich fluid inclusions. Nitrogen-rich fluid inclusions are found predominantly in the highest grade samples. Most inclusions are less then 15 μm with occasional inclusions up to 30 μm. All nitrogen-rich fluid inclusions are irregular in shape and found along planes. Kreulen and Schuiling(1982) observed $N_2$-rich fluid inclusions in rocks
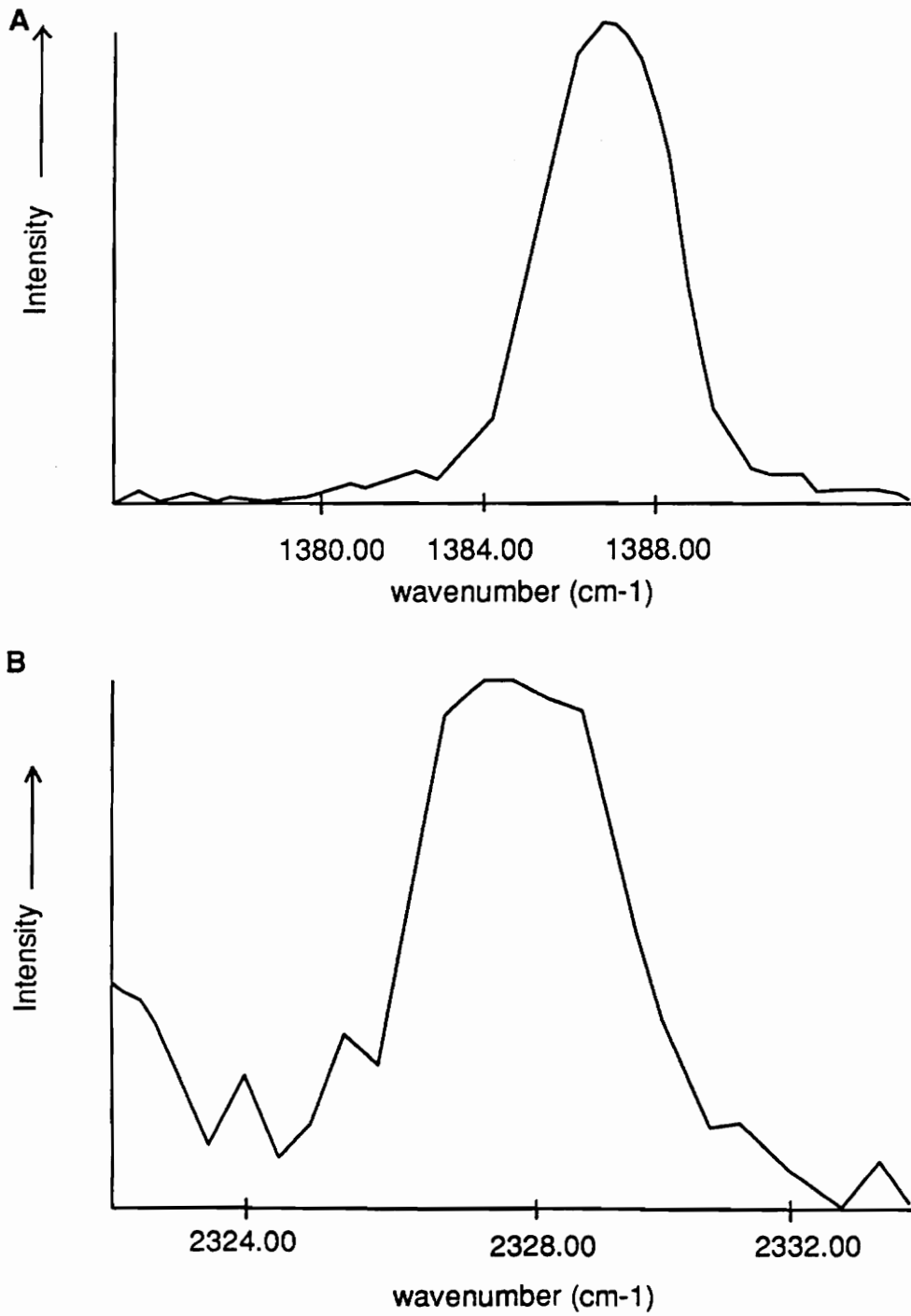
Figure 12.  Laser Raman spectra analysis of Stage B $CO_2$-$N_2$ fluid inclusions.  A) $CO_2$ peak  B) $N_2$ peak

from the Dome de l'Agout, France. They showed that under high nitrogen fugacities $N_2$ nitrogen would be the stable phase over ammonium and postulated that the nitrogen was derived from ammonium-rich micas. This may be what is occurring in south-central Massachusetts where ammonium released from micas during heating subsequently decomposed to form $N_2$-rich fluid inclusions.

Nitrogen-rich fluid inclusions show a single gas phase at room temperature. When cooled to liquid nitrogen conditions (-196°C), a rim of liquid is seen to nucleate between -150 to -160°C. Upon heating the samples the inclusions homogenized at ~-147°C (Fig 13 and 14). As the fluid inclusions approached Th, the bubble expanded, but the miniscus faded before filling the inclusion. This behavior was interpreted to be near critical homogenization behavior. Because these temperatures are just above the critical point of pure nitrogen there must be another gas species mixed with nitrogen in the inclusions, probably methane or carbon dioxide. The accuracy of measuring phase changes at these low temperatures is unknown and the error range of a few degrees may in fact be within the analytical range for the fluid inclusion stage at these temperatures. Laser Raman spectroscopic analysis reveals the presence of only a nitrogen phase (Figure 15).


Type IV, Aqueous fluid inclusions. Secondary trails of aqueous inclusions, in some cases cross cutting one another, (Figure 16) have been documented in the Coys Hill as well as in the leucosomes of sample 76228. The studied inclusions range in size from 4-30 $\mu$m. Although most of the secondary trails found do not cut grain boundaries, a few have been noted which do cut grain boundaries. These are assumed to be the latest inclusions trapped.

Crosscutting relationships were used to determine the paragenesis of aqueous inclusions. At room temperature the aqueous inclusions exhibit two phases, liquid

## Nitogen-rich Fluid Inclusions
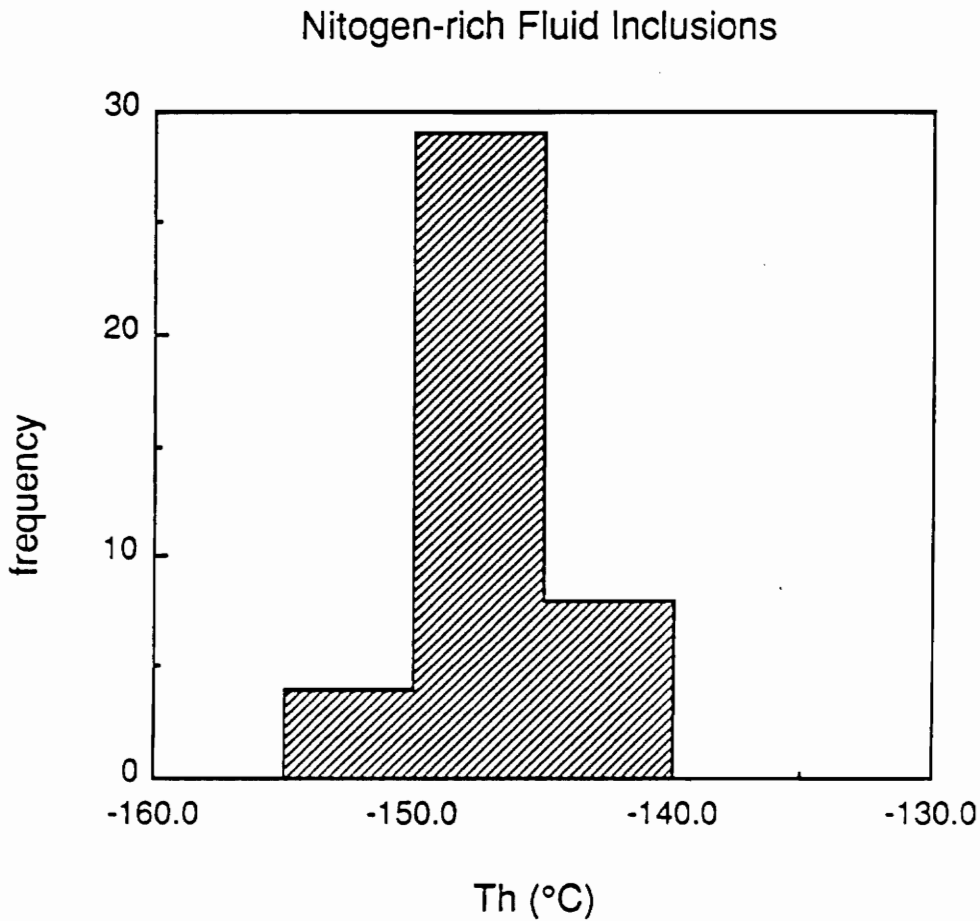


Figure 13.  Homogenization temperature  (Th °C) vs. frequency plot for $N_2$-rich fluid inclusions. The peak position is at -147°C which is the critical point of $N_2$ Scatter does exist to higher temperatures possibly indicating the presence of another gas phase but $N_2$ was the only phase revealed during laser Raman analyses.
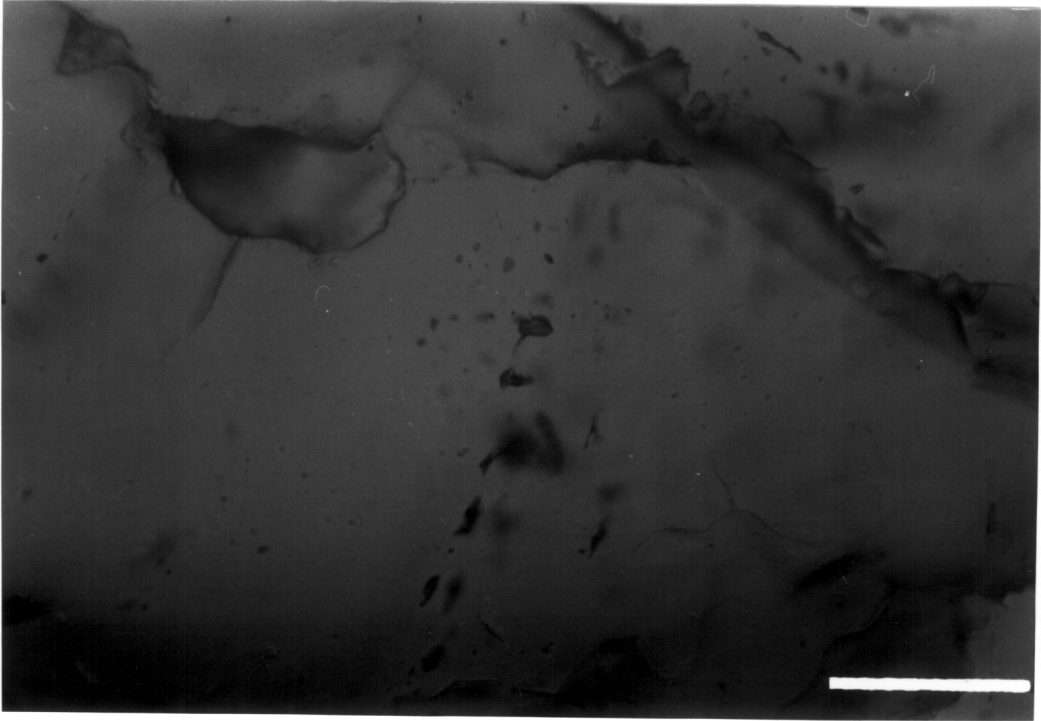
Figure 14    Plane of N$_2$-rich fluid inclusions . N$_2$ fluid inclusions are only found along planes some of which are intergranular.  Scale bar = 28 µm.
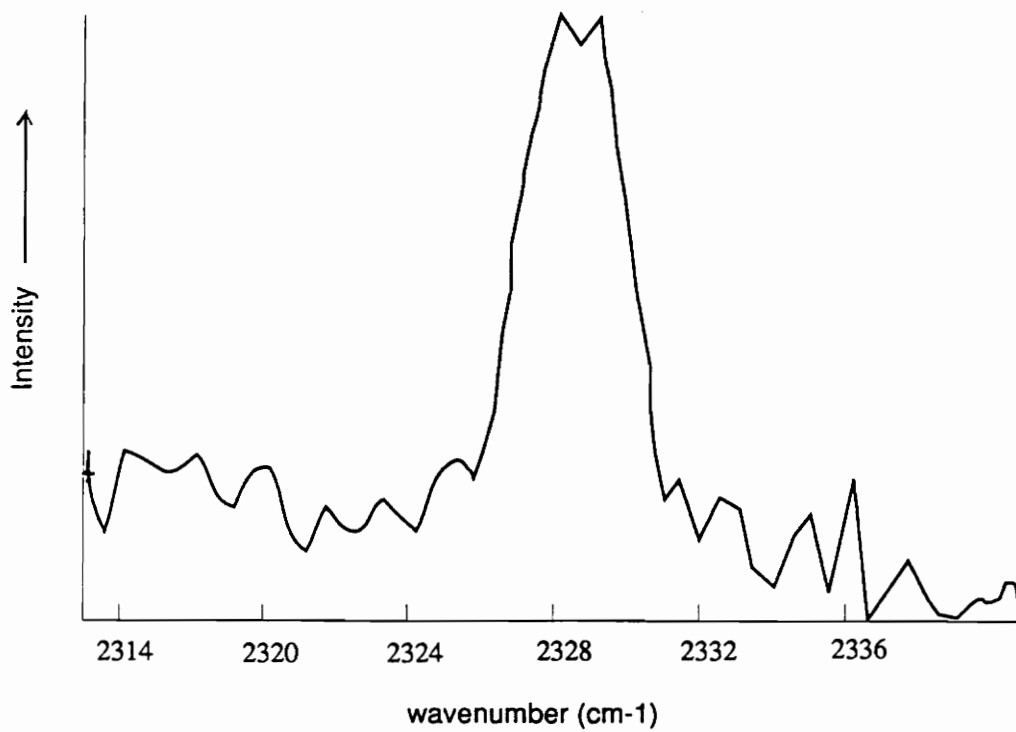
Figure 15. Laser Raman spectra for $N_2$-rich fluid inclusions from sample PL-1.
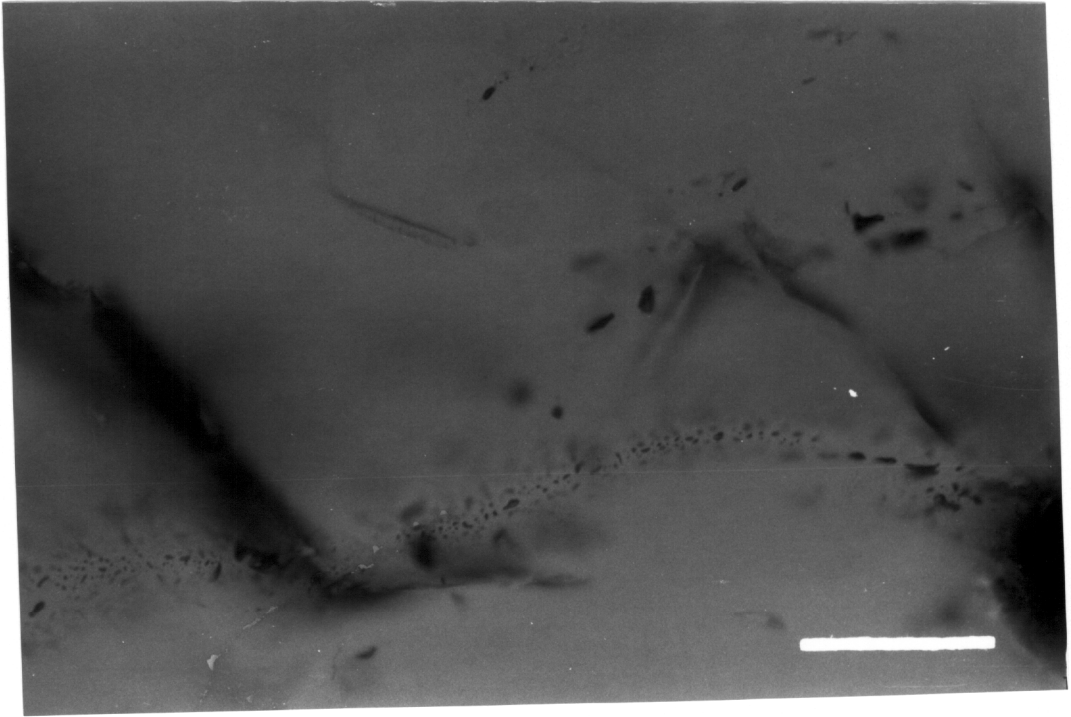
Figure 16.    Intergranular aqueous fluid inclusion trail from the Coys Hill granite.  Scale
bar = 28 μm.

(~25 %) and vapor (~75 %). Microthermometric data show the existence of four different density trails in the Coys Hill sample (Figure 9). Only a few inclusions were large enough to accurately exhibit first melting behavior. In these cases first melting of ice occurred from -22 to -27°C, indicating that NaCl is the dominant salt. Most trails from CH 1 had the same salinity (7.5 wt%) but could be divided into four groups based on homogenization temperatures. Group one trails exhibit low homogenization temperatures, in the range of 220-230°C. These trails were often only one to two inclusions thick and commonly stretched across grain boundaries. Group two trails had Th generally in the range of 325-335°C. These planes are made up of many inclusions of similar shape and size. Very similar in appearance but of different densities are Group three and four fluid inclusions. These inclusions both occur as trails, similar to type II, but homogenize at 300°C and 270°C respectively.

## DISCUSSION

### Geothermobarometry

Geothermobarometric calculations constrain the conditions of recrystallization of the mylonites relative to the sil-bio-crd gneiss host rock. Robinson *et al.*, (1989) reported pressures and temperatures for central Massachusetts using garnet-biotite thermometry and garnet-rutile-aluminosilicate-ilmenite and garnet-aluminosilicate-quartz-plagioclase barometry. Because of the higher variance of the mylonite, pressures for the mylonite were based on calculated equilibrium of garnet and cordierite. A traverse of 50 points was made from rim to rim across large porphyroblastic garnets in the coarse grained gneiss. The results (Figure 6) indicate no growth zoning and slight retrograde reequilibration, similar to garnets in other granulite terranes (Tracy, 1982). Lack of zoning in these cases has been attributed to the ability of components to diffuse through the garnet structure at high

temperatures and become homogenized (Tracy and Dietsch, 1982).

Garnets from the mylonite are more Mg rich ($X_{pyrope}$ = 0.26 -0.28) than the host rock garnets ($X_{pyrope}$ = 0.23 -0.24) (Figure 6). In order to constrain the ambient temperature during the mylonite reequilibration, biotites across the mylonite were analyzed and an attempt was made to use the biotites associated with the mylonite matrix for geothermometry. Mylonite biotites were analyzed and found to have a Fe/(Fe + Mg) of 0.29-0.34 which is markedly different than the ratio in the biotites from the host rock assemblage (0.39-0.40). The edges of the the matrix biotites show a slight decrease in the Fe/(Fe +Mg) ratio. The increase in the Fe/(Fe + Mg) ratio of garnet is thought to be controlled by the reaction

$$Kfs + crd = gar + bio$$
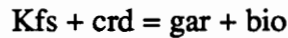
coupled with the exchange equilibrium

$$FeMg_{-1} \ gar = MgFe_{-1} \ bio.$$
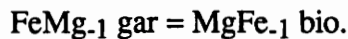
The zoning in the garnets may in fact be growth zoning with garnet growing during a temperature decrease by the reaction

$$bio \ (1) + crd + Kfs + pl =$$

$$qtz + gar + bio \ (2) + sil.$$
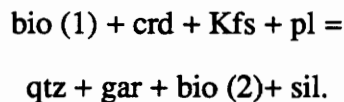
The Mn decrease towards the core of the garnet has also been suggested as indicative of growth zoning (Tracy, 1982). It is expected that using rim biotite compositions and rim garnet compositions provides a more accurate closer temperature of equilbration because biotite essentially ceases diffusion when garnet diffusion stops because no further Fe-Mg exchange reactions can take place. Also small biotites from the mylonite show compositions similar to the rim compositions of the larger biotites with no zoning and were probably the last composition in equilibrium with the garnet edge. When these compositions are used in the garnet-biotite geothermometer, temperatures of 510-540°C are

calculated.

The garnet-cordierite barometer calibrated by Thompson (1976) and Holdaway and Lee (1977) yields pressures of 7-8 kbar at 550°C for garnets and cordierites from the mylonite. This assumes that the garnet and cordierite within the mylonite are in equilibrium. If they are not in equilibrium then the pressures of Tracy and Dietsch (1982) must be used to place a constraint on the high pressure metamorphism. Their calculations using compositions of gar and crd (with gar growing within the crd) give pressures of 6.5-8 kbar at temperatures of 550°C. These pressures are in close agreement with those calculated using garnet and cordierite within the mylonite. Use of the garnet-cordierite geobarometer requires a number of assumptions (Holdaway and Lee, 1977). 1) The molar volume of cordierite is independent of its water content. 2) For a given temperature and $P_{H2O}$, water content of cordierite is independent of its composition. 3) Water content of cordierite is only a function of temperature and $P_{H2O}$ and not of $P_{tot}$. These assumptions are all related the presence of water in the cordierite structure. Holdaway and Lee (1977) have shown that in most cases these assumptions are valid, especially over most metamorphic conditions. Probably the most valid use of the garnet-cordierite barometer is when an independent temperature constraint is available and by comparing a number of different calibrations for agreement with other independent barometers. Further evidence indicating higher pressures during recrystallization of the mylonite are the loss of cordierite from the mylonite matrix and the slightly higher pyrope content of the garnets, both of which are indicative of higher pressure metamorphism.

## Fluid Inclusions

Five stages of fluid inclusion paragenesis can be determined (Figure 17) from microthermometric and petrologic evidence gathered from samples across the CMT. With

## EVIDENCE

| early | Structure and Petrology | Fluid Inclusions |
|---|---|---|

Sillimanite pseudomorphs after andalusite

Sillimanite inclusions in quartz

**Nappe stage**

Quartz included within garnet

$CO_2$ (A)

Partial melting and peak T conditions

$CO_2 \pm N_2$ (B)

**Backfold stage**

Late stage mylonites, peak P conditions

$CO_2$ (C)

**Dome stage**

Brittle deformation, microfractures cross-cutting grain boudaries

$CO_2$ (D)
aqueous (D)
$N_2$ (D)

Time (early to late)

Figure 17. This table shows petrologic and fluid inclusion evidence for the observed P-T path plotted against time. The arrows represent a range of entrapment for the inclusions Stage A are constrained to have formed before quartz was enclosed in garnet and after sillimanite was included in quartz. Stage B fluid inclusions show densities representative of peak T conditions and could have been entrapped any time before. Stage C inclusions contain high density fluids associated with the high P conditions and may have been entrapped any time before the high P stage. Type D inclusions must have formed after the formation of the mylonites because trails of fluid inclusions can be seen penetrating the mylonite.

this paragenetic sequence constraints can be placed on the P-T path of the CMT.

Decrepitation. Reequilibration of fluid inclusions occurs when the internal pressure of the inclusion differs from the confining pressure of the host mineral. This leads to a density not consistent with the density of entrapment for the fluid inclusion caused by either leaking of fluid from the inclusion or a change in volume of the inclusion. If the P-T path of a rock differs from the isochore for a fluid inclusion by a certain pressure difference then reequilbration of a fluid inclusion may occur and the isochore for that inclusion will represent a point along the P-T path of the rock. Bodnar, *et al.,* (1989) showed that decrepitation was a function of size and shape of the fluid inclusion. Through experimental work on synthetic fluid inclusions of known composition and density these workers were able to find a range of internal pressure differences at which characteristic fluid inclusions would decrepitate. Through linear regressions of the data they were able to derive a formula used to establish the internal pressure differences needed to decrepitate inclusions as a function of size and shape. Using equations presented by the authors a pressure range from which the isochores could have deviated from the P-T path and survived was calculated.

Stage A. Stage A fluid inclusions were found in quartz inclusions within xenocrystic garnets in partial melt leucosomes of sample 76228 (Figure 11). Unlike quartz, garnet is a brittle mineral which does not readily undergo crystal-plastic recrystallization. Therefore garnet may be able to shelter included quartz from crystal-plastic recrystallization and thereby enhance the ability of the quartz to preserve fluid inclusions representative of entrapment conditions. Evidence of crystal-plastic recrystallization in quartz includes undulatory extinction, subgrain formation, and reduced grain size (Hobbs *et al.,* 1976).

Quartz inclusions within garnets show no such signs of recrystallization indicating that they may be relict grains which did not undergo recrystallization or they may be completely recovered. All the inclusions homogenized to the liquid between 8.5 to 12 °C yielding a density of 0.85 g·cm$^{-3}$.

Representative isochores for these fluid inclusions pass below the peak P-T conditions (Figure 18) as recorded by garnet-biotite and garnet-cordierite geothermobarometers (Tracy *et al.,* 1976). This is to be expected since the host mineral, in this case garnet, is found within a granitic partial melt. Because the garnet is a xenocryst it probably formed before the granite melt minimum and hence before peak metamorphic conditions. Therefore, the inclusions must have formed before the rocks entered the melt region and before garnet growth. Also, fluid inclusions have been found nucleating on sillimanite inclusions (Figure 19). This establishes a lower temperature of entrapment of the $CO_2$ inclusions because, in order for a fluid inclusion to nucleate on a mineral inclusion, that mineral had to already be part of the assemblage. The early constraints on the P-T path indicate that the rocks passed from the andalusite region into the sillimanite region and then towards the granite melt minimum. Stage A inclusions thus formed after the rocks crossed into the sillimanite stability field and before melting occurred.

Calculations based on the method of Bodnar *et al.* (1989) reveal that inclusions of 8 μm in diameter within quartz can withstand internal pressure differences of 2.6 kbar. During cooling of the rocks pressure was increased to 6.5-8 kbar. This would place an internal under pressure of 3.5 kbar on the inclusions (the pressure difference between the isochore and the peak pressures). As can be seen this is 0.9 kbar more than the experimental calculations permit. Possible explanations for this discrepancy are that there are errors associated with the garnet-cordierite geobarometer. Holdaway and Lee's (1977) calibration has a 0.5 kbar uncertainty at high pressures. This range added to the inherent

Figure 18.    Progressive changes in the P-T path as defined by both petrologic and fluid

inclusion evidence.  All diagrams show Holdaway's  aluminosilicate triple point

Figure 18a shows the granite melt minimum for a water saturated melt..

a. Fluid inclusions found nucleating on sillimanite solid inclusions within

quartz inclusions in garnet.  These inclusions are constrained to have formed

between the time that andalusite was replaced by sillimanite and before the granite

melt minimum.

b. Fluid inclusion isochore for stage B inclusions which pass through the peak

metamorphic conditions.  These inclusions are found in quartz grains which do not

show signs of crystal-plastic recrystallization and may therefore preserve their fluid

inclusions.

c. High density isochore for stage C fluid inclusions associated with the late stage

mylonites.  These inclusions may represent either fluid inclusions trapped during

initial cooling and compression or the reequilibration of fluid inclusions to these

conditions.

d. Geothermobarometric evidence for the counterclockwise P-T path.  Peak

metamorphic conditions are 680-785°C at 5.6-6.3 kbar.  Late stage mylonites

which cross cut previous fabrics record conditions of 512-540°C at pressures of 7-8

kbar.  This is an actual P-T path and not a metamorphic field gradient.

e.  Stage D $CO_2$ fluid inclusions found along planes which cross cut previous

mineral lineations indicate late stage entrapment during decompression.

f.  Stage C aqueous fluid inclusions.  Cathodoluminescene has revealed a

paragenetic sequence of entrapment for these planes. as indicated by the P-T path.
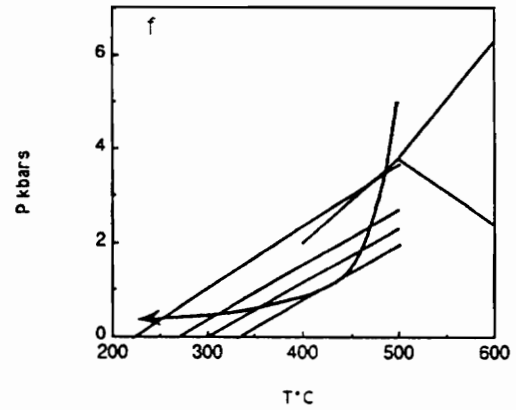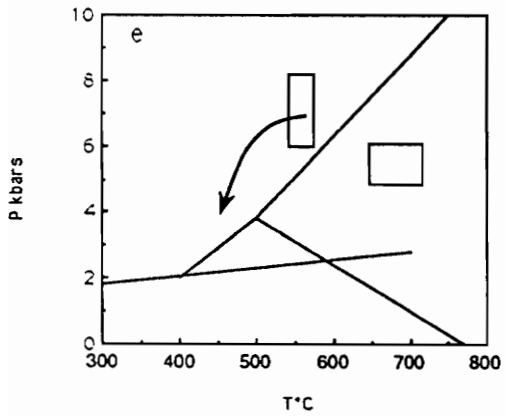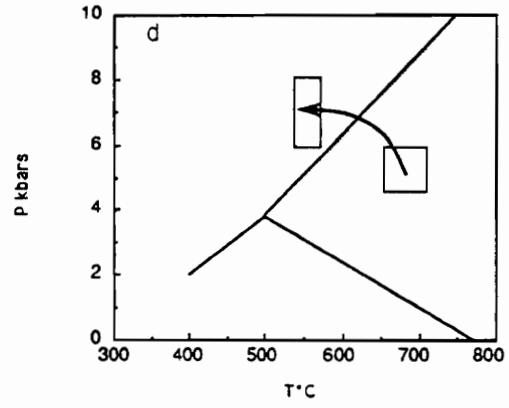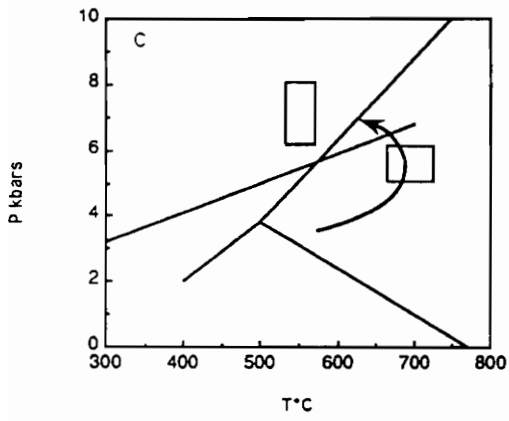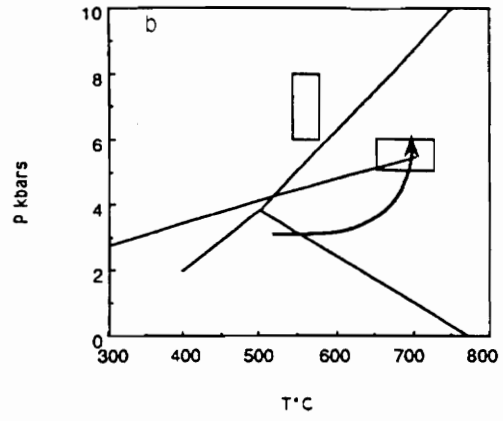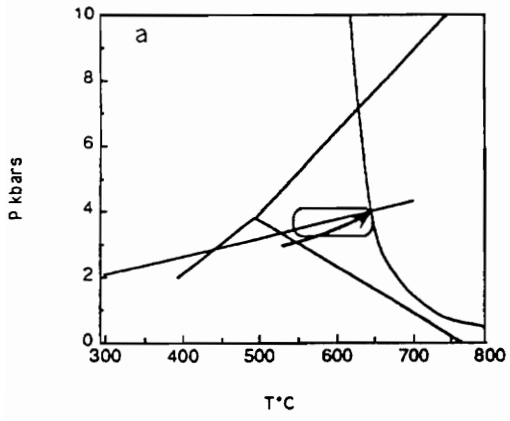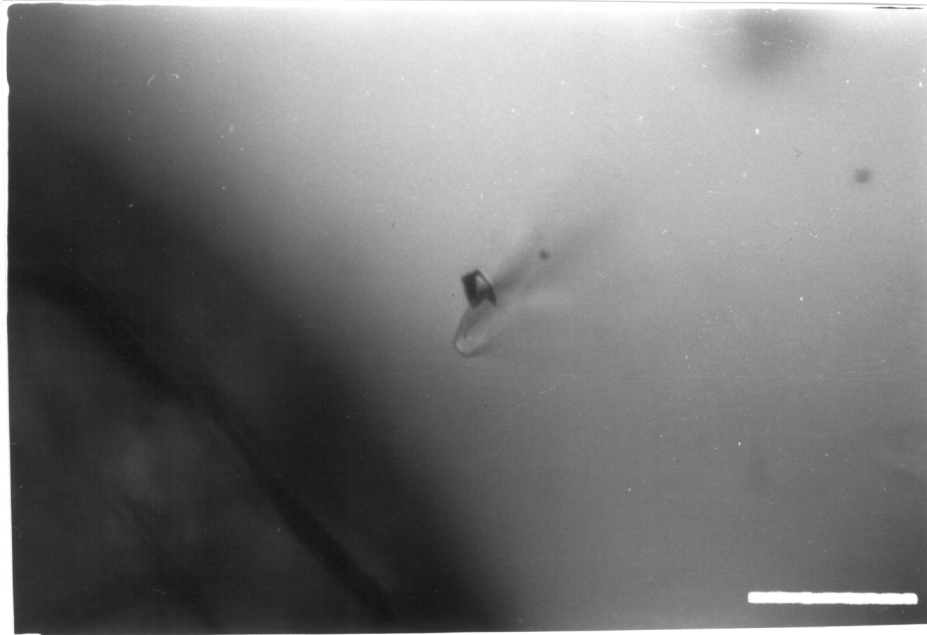
Figure 19.  Stage A fluid inclusion nucleating an a sillimanite inclusion.  These inclusions are found within a garnet xenocryst.  Scale bar = 28 μm.

error range involved in calculating isochores reveals that this 0.9 kbar difference may be within the analytical uncertainties of the techniques used. Also, it may be harder to implode an inclusion then to explode it. Imploding conditions would be prevalent during internal under pressures. This may account for the observed discrepancies in internal pressure differences.

During decompression the P-T path cannot deviate by more then 2.6 kbar from the isochore for the inclusions to survive. In fact, these inclusions exhibit no more then 2.2 kbar over pressures from the proposed P-T path and it is postulated that these fluid inclusions could have survived uplift.

Stage B. Stage B fluid inclusions were found in sample 76228 hosted in matrix quartz (Figure 10). Grains containing stage B fluid inclusions were scattered and fluid inclusions were arranged in nonplanar groups. The grains appear to be relict and show little to no undulatory extinction while most quartz grains lacking $CO_2$ inclusions showed marked undulatory extinction. These may be relict quartz grains which did not undergo crystal-plastic recrystallization and therefore have preserved their fluid inclusions (Kerrich, 1976) Microthermometric data gathered on these inclusions show them to be pure $CO_2$ with average homogenization to the liquid at -9.0°C. Isochores calculated for these inclusions pass through the peak conditions of metamorphism (Figure 18). Inclusions with this density were also found from samples Sb 10, WD 1A and WN 7

Calculations show that maximum internal pressure differences for these inclusions are on the order of 2.2 kbar. Internal under pressures created during compression are again too high but internal over pressures created during decompression do not put more than a 2 kbar pressure difference on these inclusions.

Stage C. Sample WN 7 contained stage C fluid inclusions which show a higher homogenization temperature, especially in the very small < 5 μm size range (Figure 20). Similar to stage B fluid inclusions, these inclusions occur as scattered groups with many of the higher density inclusions being completely isolated from other inclusions showing the same density. These high density fluid inclusions were associated with the late stage higher pressure mylonites and are found exclusively within a few centimeters of the mylonite. Inclusions found in this rock range in density from 0.90 to 1.04 $g \cdot cm^{-3}$ with larger inclusions showing the lower densities and the smaller inclusions showing the higher densities. Isochores for the high density fluid inclusions plot between the peak conditions of metamorphism and the conditions for the mylonites (Figure 18). No fluid inclusions could be found within the mylonite due to the fine-grained nature of the rock.

Stage C fluid inclusions may represent reequilibration of inclusions during isobaric cooling or entrapment of new fluid inclusions during compression and cooling. Owing to the small size of the highest density fluid inclusions and the larger size of the lower density inclusions, it is likely that new inclusions were trapped during isobaric cooling but due to internal pressure differences during uplift only very small inclusions could preserve their entrapment densities. Inclusions with lower densities may represent reequilibrated inclusions or inclusions formed during the peak of metamorphism, although there are no other petrologic constraints to indicate this. Perhaps the reason that inclusions with densities representative of the peak pressure conditions were not observed is because of the large internal pressure differences which would be created. Inclusions formed at these conditions would experience internal pressure differences of > 4 kbar.

Stage D. Stage D inclusions are the most abundant group of $CO_2$-rich fluid inclusions and show homogenization temperatures from 10 to 31°C. Stage D inclusions occur as both
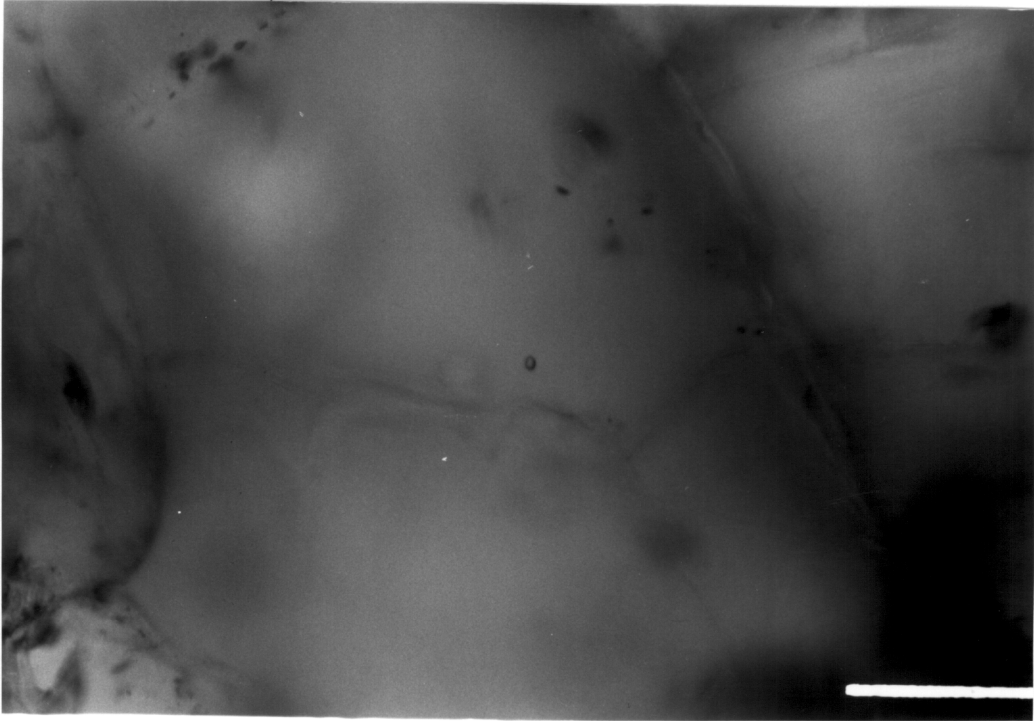
Figure 20.    Stage C  $CO_2$-rich fluid inclusions.  These fluid inclusions are found within centimeters of the late stage mylonites and show the highest densities.  Note the small size of the inclusions (<5 μm).  Scale bar = 28 μm.

intragranular and intergranular trails. Inclusions within trails frequently exhibit irregular shape and are large (>15 $\mu$m) with some as large as 50 $\mu$m (Figure 21). The densities of these inclusions range from 0.85 to 0.20 g·cm$^{-3}$.

These trails probably represent a $CO_2$-rich fluid that was liberated during decrepitation and reequilibration of inclusions and subsequently entrapped along microfractures. The microfractures cut all previously produced fabrics including the late stage mylonite where a $CO_2$-rich fluid inclusion trail can be seen cutting into the fine grained mylonite before terminating. Inclusions of these densities provide us with a late stage path for the rocks to pass through, knowing that the path must intersect the representative isochore for the inclusions (Figure 18).

Also in stage D are abundant aqueous inclusions found only in planes and never in nonplanar groups or as isolated individuals. Inclusion planes were analyzed individually to define the paragenetic sequence of entrapment where trails cross cut one another. Where trails of different composition or density did cross cut one another, cathodoluminescence maps were made of the trails to elucidated the fluid inclusion paragenesis. Inclusions from CH 1 showed four different density fluid inclusion trails which cross cut one another. Trails with representative densities of 0.89 g·cm$^{-3}$ and 0.74 g·cm$^{-3}$ (Figure 22) were found to cross cut one another and trails with representative densities of 0.80 g·cm$^{-3}$ and 0.84 g·cm$^{-3}$ (Figure 23) were also found to cross cut. The highest density trails were long and not wider than one or two inclusions thick. When cathodoluminescence maps were made of these trails a striking luminescence difference was observed between the host qtz and the healed qtz along the fractures.

Of the two pairs of crosscutting fluid inclusion planes recognized it was found that CL maps of these trails reveal that the trail which trends northeast-southwest (0.74 g·cm$^{-3}$) is crosscutting and overprinting the trail trending northwest-southeast
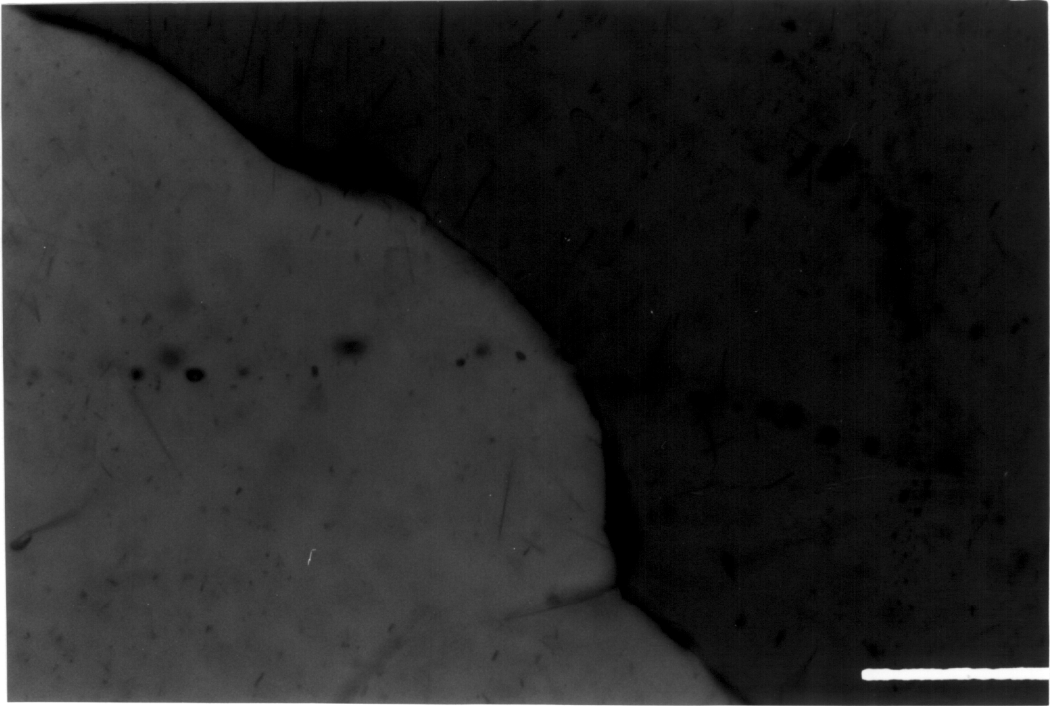
Figure 21.    Stage D $CO_2$-rich fluid inclusions.  These fluid inclusions are found along intergranular trails which cross cut all previous fabrics including the late stage mylonites.  Scale bar = 28 $\mu$m.
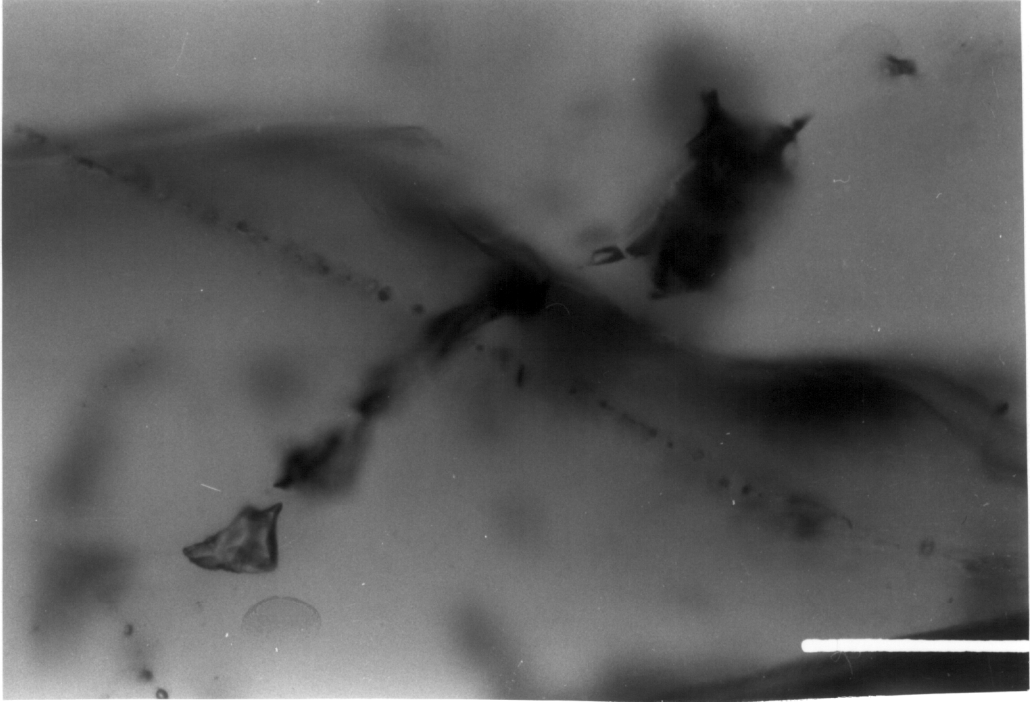
Figure 22.    Aqueous fluid inclusion planes corresponding to cathodoluminescence map
              shown in 24A.  The Figure shows planes of inclusions one NE-SW and
              the other ~E-W crosscutting one another.  The NE-SW trending trail
              formed after the east-west trending trail as revealed by
              cathodoluminescence.  Scale bar = 28 μm.
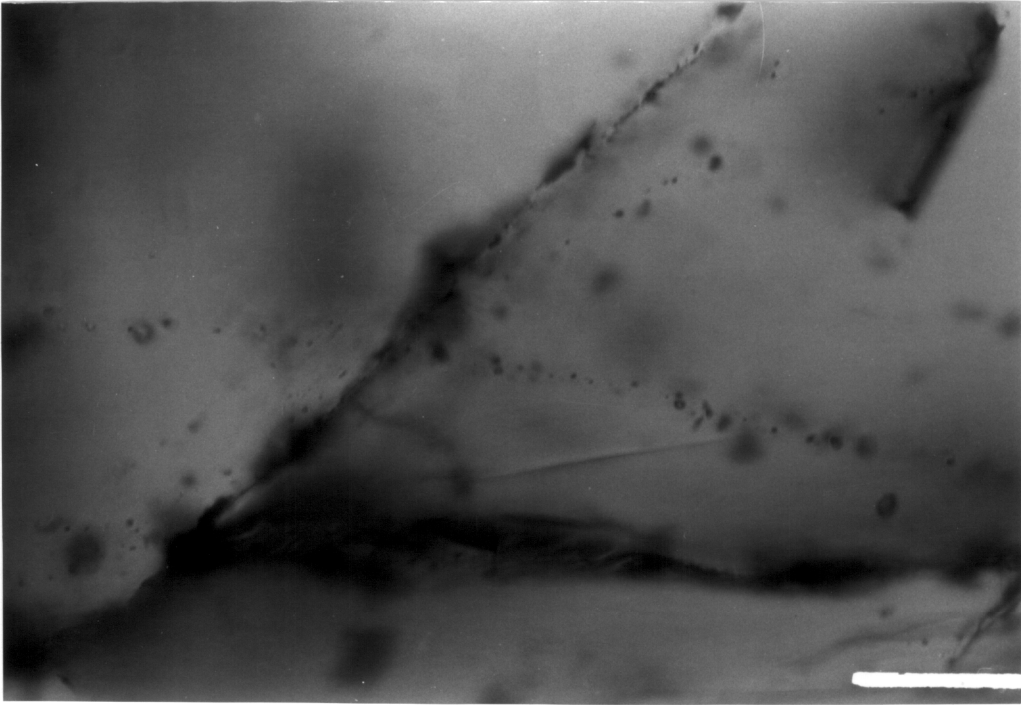
Figure 23. Aqueous fluid inclusion planes corresponding to cathodoluminescence maps shown in Figure 24B. The Figure shows planes of inclusions one NE-SW and the other E-W crosscutting one another. The NE-SW trending trail formed after the roughly east-west trending trail as revealed by cathodoluminescence. Scale bar = 28 μm.

A
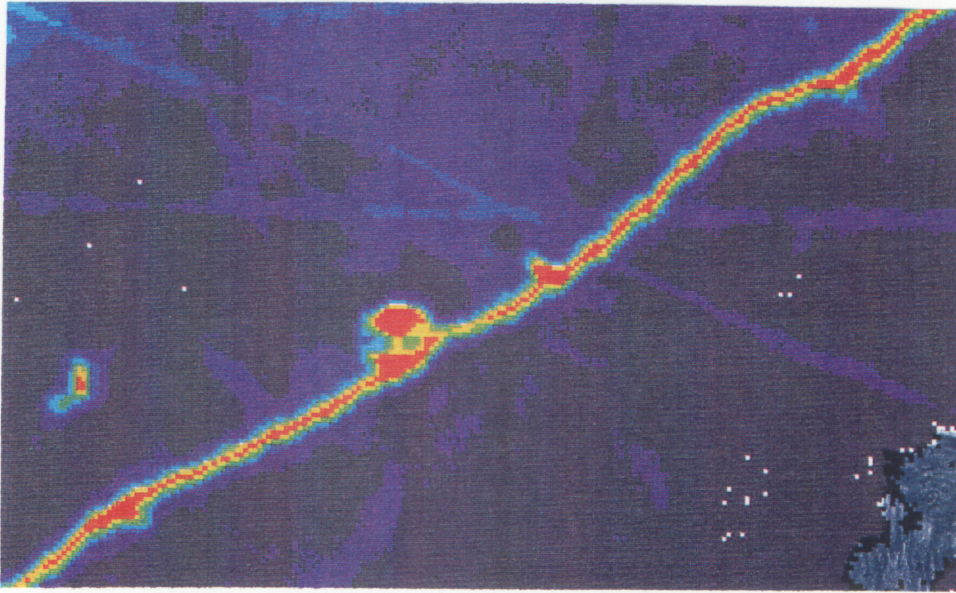


B
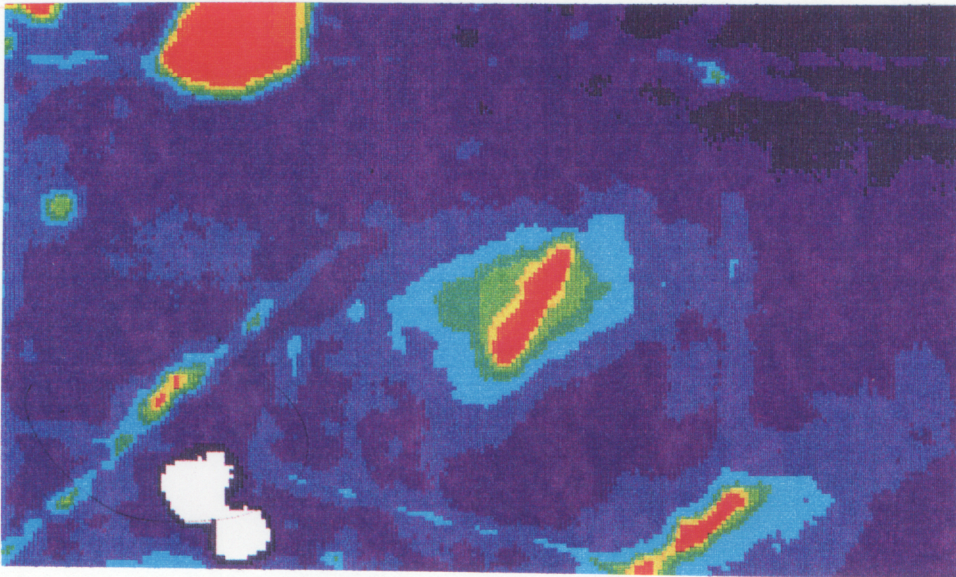


Figure 24.  A.  Cathodoluminescence map corresponding to Figure 22.  With the aid of
cathodoluminescence a paragenetic sequence of entrapment can be
determined.  In this case it can be seen from the over printing of
cathodoluminescent properties that the NE-SW trending trail formed later then
the faint E-W trending trail.
B.  In this map it is seen that the NE-SW trending trail also formed after the
E-W trending trail. Scale bar = 28 µm.

(0.89 g·cm$^{-3}$) (Figure 24), hence the low density trail has formed before the high density trail. This is the opposite of what would be expected for isothermal decompression. In pair two the crosscutting relationships are harder to determine but in the lower left corner the trail trending northeast-southwest (0.80 g·cm$^{-3}$) formed after the trail trending roughly east-west (0.84 g·cm$^{-3}$). This entrapment order helps to constrain the later part of the P-T path because during decompression it must intersect a point along each of the aqueous isochores in the order in which they were entrapped. The first set of fluid inclusions to be entrapped would be the 0.84 g·cm$^{-3}$ set. This is followed by entrapment of 0.80 g·cm$^{-3}$, and 0.74 g·cm$^{-3}$ and finally 0.89 g·cm$^{-3}$ inclusions (Figure 18).

$N_2$-rich fluid inclusions were also entrapped during the late stage. Microthermometry and Raman spectroscopy suggest densities near the critical point of nitrogen. Isochores for $N_2$ inclusions of these densities would project far below the temperatures of metamorphism. This combined with the occurrence of the fluid inclusions, usually along trails suggests that they were entrapped late in the paragenetic sequence or reequilibrated to later conditions towards the end of uplift.

## IMPLICATIONS FOR P-T PATH

Fluid inclusion and petrologic data collected in this study support earlier models of a counterclockwise P-T trajectory in the CMT of south-central Massachusetts (Fig 25). The terrane has undergone an initial high-T, low-P (Buchan-type) metamorphism followed by a low-T, high-P metamorphism. Peak conditions of the high temperature metamorphism reached 685-780°C and pressures of 5.6-6.3 kbar, while, the high-P metamorphism occurred at 510-540°C at pressures of 7-8 kbar. Thermobarometric calculations are consistent with petrologic evidence including probable sillimanite pseudomorphing andalusite, the presence of cordierite in pelitic lithologies, replacement of

# P-T TRAJECTORY
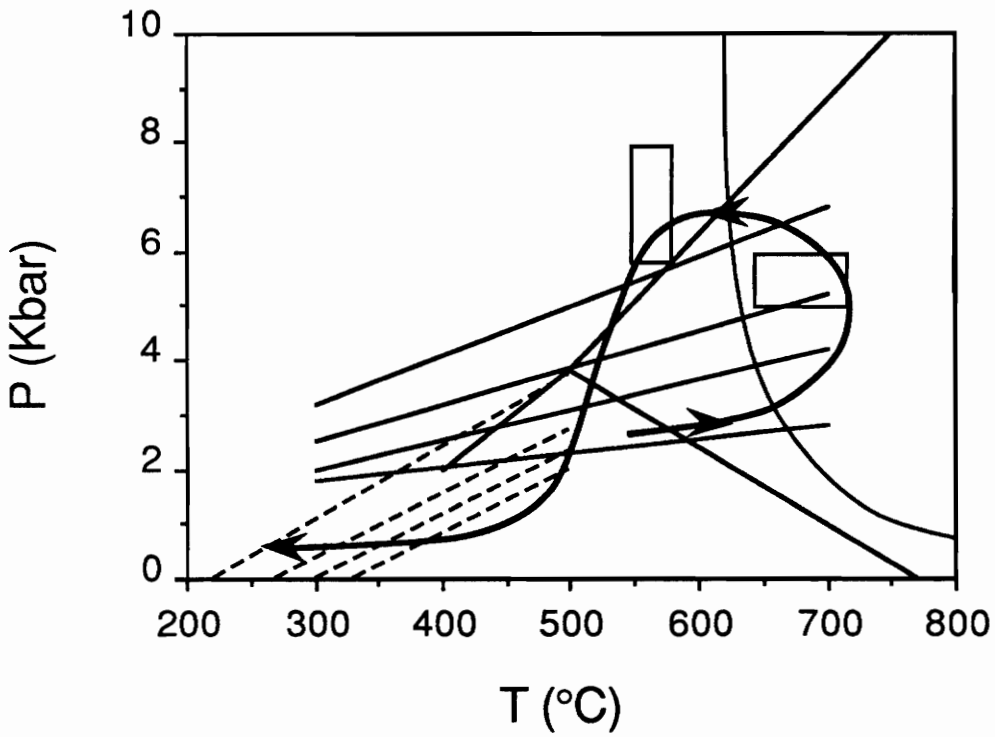


Figure 25. The path shows an early high-T, lower P metamorphism followed by a later lower-T, higher P metamorphism. The end of metamorphism was accompanied by isothermal decompression constrained by the entrapment order of the late stage aqueous fluid inclusions.

low-P assemblages with high-P assemblages and the recrystallization of late stage mylonites to high pressure conditions. In order to account for this metamorphism high crustal temperatures are required. These elevated temperatures are evidenced by abundant partial melting and intrusive activity as well as by anomalously high radiogenic material in the rocks of the CMT (Chamberlain and Sodnar, 1991). The emplacement of large numbers of intrusions in the crust is represented by abundant plutons further to the north in the CMT. The northern part of the CMT is thought to represent shallower crustal levels than the southern part of the belt and represents the section of the crust where intrusions ponded during their ascent.

Four stages of fluid inclusion entrapment have been documented in rocks of the area. Stage A consisted of the entrapment of $CO_2$ fluids during prograde metamorphism and isobaric heating. These inclusions are constrained to have been trapped between the formation of sil and the formation of granitic melt. A second stage of fluid entrapment occurred at peak conditions of metamorphism. $CO_2$ inclusions found in partial melts have densities representative of peak conditions. Stage C entrapment consisted of high density $CO_2$ inclusions during compression and cooling. Isochores plotted for these inclusions project between the conditions of formation for the mylonites and peak metamorphic conditions. Stage D of fluid entrapment occurred during isothermal decompression and is characterized by low density aqueous and $CO_2$-rich fluid inclusion trails, some of which crosscut grain boundaries and aqueous fluid inclusion trails.

# References

Armstrong, T.R., Tracy, R.J. and Hames, W.E., in review, Contrasting styles of Taconian, eastern Acadian, and western Acadian metamorphisms, central and western New England. Journal of Metamorphic Geology

Ashwall, L.D., Leo, G.W., Robinson, P., Zartman, R.E. and Hall, D.J., 1979, The Belchertown qtz monzodiorite pluton, west-central Massachusetts, a syntectonic Acadian intrusion. American J. of Science, v. 35, p.191-198.

Barriero, B. and Aleinikoff, J.N., 1985, Sm-Nd and U-Pb isotope relationships in the Kinsman qtz monzonite, New Hampshire. GSA Abstracts with Programs, v. 17, p. 3.

Bodnar, R.J., 1985, Pressure-volume-temperature-composition (PVTX) properties of the system $H_2O$-NaCl at elevated temperaures and pressures. Ph.D. dissertation, Pennsylvania State University. 183p.

Bodnar, R.J., Binns, P.R. and Hall, D.L., 1989, Synthetic fluid inclusions-VI. Quantitative evaluation of the decrepitation behavior of fluid inclusions in qtz at one atmosphere confining pressure. Journal of Metamorphic Petrology, v. 7, p. 229-241.

Chamberlain, C.P. and Sodnar, L.J., 1991, The effects of heat producing elements on the evolution of the New England appalachians. Northeast GSA, abstracts and programs, v. 23, no. 1, Baltimore, Md.

Deer, W.A., Howie, R.A. and Zusman, J., 1976, Rock forming minerals, Ortho and Ring silicates. London, 528p.

England, P.C. and Richardson, S.W., 1977, The influence of erosion upon the mineral facies of rocks from different metamorphic environments. Geologic Society of London Journal, v. 134, p. 201-213.

Fisher, G., 1989, Matrix analysis of metamorphic mineral assemblages and reactions. Contributions to Mineralogy and Petrology, v. 102, p. 69-77.

Ferry, J.M. and Spear, F.S., 1978, Experimental calibration of the partitioning of Fe and Mg between gar and bio. Contributions to Mineralogy and Petrology, v. 66, p. 113-117.

Guidotti, 1984, Micas in metamorphic rocks. In Bailey, S.W., ed., Mineralogical Society of America Reviews in Mineralogy, v. 42, p. 33-41.

Hall, D.L., Sterner, S.M. and Bodnar, R.J., 1988, Freezing point depressions in the NaCl-KCl-$H_2O$ system. Journal of Economic Geology, v. 83, p. 197-207.

Hames, W.E., Tracy, R.J. and Bodnar, R.J., 1989, Post metamorphic unroofing history as deduced from petrology, fluid inclusions, thermochronometry and thermal modeling: an example from southwestern-New England. Geology, v. 17, p. 727-730.

Hatch, N.L., Moench, R.H. and Lyons, J.B., 1983, Silurian-Lower Devonian stratigraphy of eastern and south-central New Hampshire: extensions from western Maine. American Journal of Science, v. 283, p. 739-761.

Hatch, N.L., Zen, E-an., Goldsmith, R., Ratcliffe, N., Robinson, P., Stanley, R. and Wones D., 1984, Lithotectonic assemblages as portrayed on the new bedrock geologic map of Massachusetts. American J. of Science, v. 284, p. 1026-1034.

Heinrich, K.F.J., 1981, Electron beam X-ray microanalysis. New York: Van Nostrand Reinhold and Company, 578 p.

Hobbs, B.E., Means, W.D. and Williams, P.F., 1976, An outline of structural Geology. John Wiley and Sons, New York, 571 p.

Hodges. K.V. and Crowley, P.D., 1985, Error estimation and empirical geothermobarometry for pelitic schists. American Mineralogist, v. 70, p. 702-709.

Holdaway, M.J. and Lee, S.M., 1977, Fe-Mg crd stability in high grade pelitic rocks based on experimental, theoretical and natural observations. Contributions to Mineralogy and Petrology, v. 63, p. 175-198.

Holloway, J., 1981, Compositions and volumes of supercritical fluids in the earth's crust. In, Hollister, L.S. and Crawford M.J., ed. Mineralogical Association of Canada, Short Course in Fluid Inclusions: Application to Petrology, Calgary. 304p.

Hollister, L.S., Burruss, R.C., Henry, D.L., Hendal, E.M., 1979, Physical conditions during uplift of metamorphic terranes, as recorded by fluid inclusions. Bull. Mineral., v. 102, p. 555-561.

Kerrich, R., 1976, Some effects of tectonic recrystallization on fluid inclusions in vein quartz. Contributions to Mineralogy and Petrology, v. 59, p. 195-202.

Kreulen, R. and Schuiling, R.D., 1982, $N_2$-$CH_4$-$CO_2$ fluids during formation of the Dome de l'Agout, France. Geochemica et Cosmocica Acta, v.46, p. 191-203.

Lyons, J.B. and Livingston, D.E., 1977, Rb-Sr age of the New Hampshire plutonic series. Geologic Society of America Bulletin, v. 66, p. 105-146.

Moench, R.H., and Aleinifkoff, J.N., 1991, The Piermont allochthon of northern New England: A displaced remnant of a post-Taconian extensional sub-basin marginal to the central Maine trough. NEGSA Abstracts with Programs, v. 23, no. 1.

Robinson, P. and Hall, L.M., 1980, Tectonic synthesis of southern New England. In Wones, D.R., ed., the Caledonides in the USA. IGCP Project 27, Caledonide Orogen, p. 73-82. Blacksburg Va.

Robinson, P., Tracy, R.J., Hollocher, K., Berry, H.N. and Thompson, J.A., 1989, Baement and cover in the Acadian metamorphic high of central Massachusetts. Chamberlain, C.P. and Robinson, P., ed., Styles of Acadian metamorphism with depth in the central Acadian high, New England. p. 69-138. Amherst Massachusetts.

Shearer, C.K. and Robinson, P., 1980, Constant temperature metamorphism of an $H_2O$ activity gradient in a prexisting contact aureole. EOS v. 61, p. 389.

Stout, M.Z., Crawford, M.L. and Ghent, E.D., 1986, Pressure-temperature and evolution of fluid compositions of $AL_2SiO_5$-bearing rocks, Mica Creek, B.C., in light of fluid inclusion data and mineral equilibria. Contributions to Mineralogy and Petrology, v. 92, p. 236-247.

Tucker, R.D. and Robunson, P., 1990 Age and setting of the Bronson Hill magmatic arc: A re-evaluation based on U-Pb zircon ages in southern New England. Geological Society of America Bulletin. v. 102, no. 10, p. 1404-1419.

Thompson, J.B., Jr., Robinson P., Clifford, T.N. and Task, N.J., 1968, Nappes and gneiss domes in central New England. In Zen, E-an, White, W.S., Hadley, J.B. and Thompson, J.B., Jr., eds. Studies of Appalachian Geology: Norhtern and Maritime, p. 203-218, Interscience Publishers, New York

Thompson, A.B., 1976, Mineral reactions in pelitic rocks: II. Calculations of some P-T-X(Fe-Mg) phase relations. American J. of Science, v. 276, p. 425-454.

Tracy, R.J., 1982, Compositional zoning and inclusions in metamorphic minerals. Ferry, J.M. ed. Characterization of metamorphism through mineral equilibria. in Reviews in Mineralogy. p. 355-397, Chelsea, Michigan.

Tracy, R.J. and Dietsch, C., 1982, High temperature retrograde reactions in pelitic gneiss, central Massachusetts. Canadian Minerologist, v. 20, p. 425-439.

Tracy, R.J., Hames, W.E., Armstrong, T.R. and Miller, S.J., 1991, Contrasting styles of Taconian, eastern Acadian and western Acadian metamorphisms, central and western New England. NEGSA Abstracts and Programs, v. 21, no. 1.

Tracy, R.J. and Robinson, P. and Thompson, A.B., 1976, Garnet composition and zoning in the determination of temperature and pressure of metamorphism, central-Massachusetts. American Mineralogist v. 61, p 762-775

Tracy, R.J. and Robinson, P., 1980, Evolution of metamorphic belts: information from detailed petrologic studies. In Wones, D.R., ed., the Caledonides in the USA. IGCP Project 27, Caledonide orogen, p. 189-195. Blacksburg Va.

Zeitler, P.J., Barreiro, B., Chamberlain, C.P., Rumble, D. III, 1990, Ion-microprobe dating of zircon from quartz-graphite veins at the Bristol, New Hampshire, metamorphic hot spot. Geology, v.18, p. 626-629

# APPENDIX I  SAMPLE DESCRIPTION

## Petrographic Description

WD-1 and 1A. This is a dark amphibolite gneiss of the Partridge Formation with partial melt segregations along the foliation. The sample contains three prominent divisions: amphibolite, a sheared zone and a partial melt segregation. The rock has an assemblage of a brownish cummingtonite-bio-hbl-gar-pl and qtz.

The shear zone is made up of the assemblage bio-qtz-pl-gar and sil. Biotite is the dominant matrix mineral displaying a fine grained recrystallized texture and a prominent shear sense along with lesser amounts of quartz and plagioclase. Large porphyroclasts of garnet and feldspar with the foliation wrapping around them, indicate that the clasts predate deformation. Euhedral apatites are found in the foliation and definitely crosscut the existing foliation. While the big clasts of garnet seem to predate the deformation these small apatites seem to be postectonic or syntectonic.

CH-1. The Coys Hill granite is a Devonian granite which has undergone Acadian deformation and metamorphism. The assemblage recorded in the sample is qtz-bio-gar sil-pl ± gr. This is the typical assemblage of zone 5. A pronounced foliation has developed during deformation and is marked by orientation of biotites and large relict phenocrysts of K-feldspar.

WN-5. This is the common sulfidic schist of the Rangeley Formation. The outcrop is severely weathered but fresh samples can be gathered. The assemblage here is a typical zone 6 assemblage of qtz-Kfs-pl-bio-gar-crd-sil-gr-ilm and po.

WN-7. Within the Rangeley Formation are numerous recrystallized mylonites thought to have formed at the end of the backfold stage of deformation. These mylonites are of particular importance in determination of the proposed P-T trajectory. Because the mylonites cross cut all previous foliations and preserve dome stage folds within them (Robinson *et al.*, 1989) they probably represent conditions prevalent during the later stages of metamorphism. The mylonite considered here is from sample WN-7 and has been studied in great detail by Robinson *et al.,* (1989).

In this study the mylonite was examined and compared with the granulite host rock. The host rock assemblage is bio-pl-crd-gar-Kfs and sil with po and apt as accessory minerals. Within the mylonite, biotite is the most abundant mineral but decreases in concentration away from the mylonitic band. Outside the band biotite occurs as scattered patches. Grain size in the host rock steadily coarsens away from the mylonite, reaching a maximum grain size of 1.6 mm.

The mylonite zone contains the assemblage garnet, biotite, sillimanite, feldspar and quartz with clasts of cordierite and feldspar. Garnets growing in the mylonite do not quite achieve an euhedral crystal form. Definite euhedral qualities can be seen in some of the garnets but many embayments exist in others, thereby destroying the euhedral nature of the minerals. The porhyroblastic nature of the garnets as well as some oriented inclusions suggest that they grew during or after recrystallization of the mylonite (Robinson *et al.,* 1989). because relict garnets would show signs of fracturing and crushing as well as a foliation wrapping around the clasts. Some garnets appear to be euhedral crystals. The cordierite is of an assemblage produced before the growth of the garnets. Whereas the garnets crosscut the foliation, cordierite occurs as clasts within the mylonite.

WN-7A. This rock is a gray weathering gneiss of the Rangeley Formation. This rock, which has been collected from the same sample locality as WN-7, does not have the fine grained mylonite. Although the assemblages are the same the textures are different.

This rock is characterized by long *stretched out* garnets. Garnet, being a hard and brittle mineral, does not grow in these elongate textures. In thick section it appears that the garnet is a continuous growth. But, looking more closely, the garnet appears to be a conglomerate of several different garnets.

Shearing and deformation-enhanced recrystallization is evidenced by quartz fabrics. In the zone with the garnets there is a reduction in grain size and an increase in abundance of quartz. The quartz grains show intense undulatory extinction and subgrain, core and mantle, development. Also, albite twinning in the feldspars are distorted and bent.


76639 This sample is a leucocratic rock thought to have originated through the partial melting of the host gneiss. The leucosomes contain qtz-Kfs-pl-gar and sil with minor cordierite. Around the leucosomes are dark layers consisting of gar-bio-crd and sil. These layers are thought to be a restite. Garnets within the leucosome are vary from 20 microns to a few millimeters.


Sb-10. This is a gray biotite, garnet and cordierite granulite of the Paxton Formation with lenses of calc-silicate granulite. The sample studied contains the assemblage bio-gar-crd-Kfs-qtz and sil. An interesting textural aspect of this sample occurs in the K-feldspars. Many of the K-feldspars show exsolution lamellae, microperthitic and myrmicitic textures. Within the sample are a few large muscovites. These are assumed to be a retrograde mineral which formed through the reaction of sillimanite, k-feldspar and water.. This is one of the few occurrences of muscovite in the central Massachusetts Acadian high.

WL-9. This sample area has two lithologies of interest. The majority of the outcrop is composed of a two pyroxene granulite. The assemblage present here is qtz-Kfs-opx-cpx-, bio-ilm-pl and secondary cummingtonite and hbl. Also present are pods of calc-silicate pegmatite with the assemblage cc-di-qtz-pl-spn-ap, and scp (Robinson *et al.*, 1989).

PL-1. This sample was collected from the pipeline excavation (see Robinson *et al.*, 1989) across strike in southern Massachusetts. The sample contains the assemblage qtz-Kfs-pl-gar-bio-crd-sil and ilm. Within the sample are large porphyroblasts of garnet with quartz pressure shadows around them. Biotite and sillimanite define a foliation wrapping around the blasts. Within many of the garnets are inclusions of quartz and fibrolitic sillimanite while outside the garnet both prismatic and fibrolitic sillimanite are present.

## APPENDIX II FLUID INCLUSION DATA

All fluid inclusions analyzed are presented below in table form. The tables lists melting temperature ($Tm°C$), homogenization temperature ($Th°C$), phase to which it homogenizes and size.

$CO_2$ fluid inclusions

| Tm(°C) | Th(°C) | phase | size(μm) | shape |
|--------|--------|-------|----------|-------|
| -56.8 | 9.5 | L | 8 | negative |
| -56.7 | 10.8 | L | 7 | negative |
| -56.9 | 9.4 | L | 7 | negative |
| -57.1 | 9.5 | L | 6 | negative |
| -56.6 | 9.4 | L | 9 | negative |
| -56.7 | 9.3 | L | 10 | negative |
| -56.6 | 9.2 | L | 8 | negative |
| -56.6 | 9.4 | L | 6 | negative |
| -56.6 | 8.6 | L | 7 | negative |
| -56.9 | 9.8 | L | 7 | negative |
| -56.7 | 8.8 | L | 11 | negative |
| -56.7 | 9.2 | L | 6 | negative |
| -56.6 | 9.0 | L | 8 | negative |
| -56.6 | -9 | L | 12 | negative |
| -56.6 | -8.8 | L | 10 | negative |
| -56.7 | -9.1 | L | 10 | negative |
| -56.6 | -8.9 | L | 8 | negative |
| -56.7 | -8.8 | L | 15 | negative |
| -56.7 | -7.6 | L | 9 | negative |
| -56.6 | -8.5 | L | 10 | negative |
| -56.9 | -8.2 | L | 8 | negative |
| -56.7 | -9.3 | L | 5-12 | negative |
| -56.6 | -5.6 | L | 8 | negative |
| -56.6 | -7.2 | L | 8 | negative |
| -56.6 | -7.3 | L | 10 | negative |
| -57.1 | -7.8 | L | 10 | negative |
| -56.6 | -8.2 | L | 8 | negative |
| -56.6 | -8.2 | L | 8 | negative |
| -56.6 | -7.7 | L | 8 | negative |
| -57.1 | -7.5 | L | 8 | negative |
| -57.0 | -7.6 | L | 10 | negative |
| -56.8 | -7.3 | L | 12 | negative |
| -56.8 | -6.7 | L | 5 | negative |
| -56.6 | 30.5 | V | <25 | irregular |
| -56.6 | 28.9 | V | <25 | irregular |
| -56.6 | 29.7 | V | 20 | irregular |
| -56.7 | 31.3 | V | 15 | irregular |
| -56.6 | 30.8 | V | 15 | irregular |
| -56.6 | 30.7 | V | 20 | irregular |

| Tm(°C) | Th(°C) | phase | size(μm) | shape |
|--------|--------|-------|----------|-------|
| -56.6 | 19.2 | L | 25 | irregular |
| -56.6 | 19.3 | L | 25 | irregular |
| -56.6 | 19.7 | L | 25 | irregular |
| -56.6 | 19.6 | L | 15 | irregular |
| -56.6 | 20.8 | L | 15 | irregular |
| -57.2 | 19.9 | L | 15 | irregular |
| -56.6 | 19.2 | L | 25 | irregular |
| -56.8 | 19.8 | L | 20 | irregular |
| -56.6 | 30.8 | V | 15 | irregular |
| -56.7 | 30.5 | V | 25 | irregular |
| -56.6 | 28.9 | V | 25 | irregular |
| -56.6 | 29.5 | V | 25 | irregular |
| -56.6 | 26.8 | V | 25 | irregular |
| -56.6 | 26.7 | L | 25 | irregular |
| -56.6 | 13.9 | L | 15 | irregular |
| -56.6 | 13.9 | L | 15 | irregular |
| -56.6 | 13.8 | L | 15 | irregular |
| -56.6 | 14.0 | L | 15 | irregular |
| -56.7 | 13.5 | L | 15 | irregular |
| -56.7 | 11.1 | L | 15 | irregular |
| -56.6 | 12.7 | L | 18 | irregular |
| -56.8 | 10.4 | L | 10 | irregular |
| -57.0 | 11.1 | L | 15 | irregular |
| -57.1 | 14.5 | L | 20 | irregular |
| -56.8 | 14.2 | L | 10 | irregular |
| -56.6 | 19.0 | L | 25 | irregular |
| -56.7 | -1.4 | L | 10 | irregular |
| -56.7 | -23 | L | 3 - 5 | negative |
| -56.5 | -24.4 | L | 3 - 5 | negative |
| -56.8 | -25.5 | L | 3 - 5 | negative |
| -56.9 | -29.8 | L | 3 - 5 | negative |
| -56.7 | -22.3 | L | 3 - 5 | negative |
| -56.6 | -22.5 | L | 3 - 5 | negative |
| -56.9 | -19.0 | L | 3 - 5 | negative |
| -57.2 | -25.6 | L | 3 - 5 | negative |
| -57.6 | -26.2 | L | 3 - 5 | negative |
| -56.6 | -22.3 | L | 3 - 5 | negative |
| -56.7 | -25.6 | L | 3 - 5 | negative |
| -56.7 | 13.3 | L | 13 | oval |
| -56.8 | -9 | L | 5 - 10 | oval |
| -58.9 | -9.3 | L | 5 - 10 | oval |
| -56.8 | -9.4 | L | 5 - 10 | oval |
| -56.6 | -9.2 | L | 5 - 10 | oval |
| -56.6 | -9.5 | L | 5 - 10 | oval |
| -56.7 | -9.4 | L | 5 - 10 | oval |

| Tm(°C) | Th(°C) | phase | size(µm) | shape |
|--------|--------|-------|----------|----------|
| -56.7 | -22.2 | L | 5 | oval |
| -56.6 | -24.4 | L | 5 | oval |
| -57.2 | -18.5 | L | 5 | oval |
| -57.1 | -0.2 | L | 10 | oval |
| -56.8 | -0.8 | L | 15 | oval |
| -56.7 | -0.4 | L | 10 | oval |
| -56.8 | -0.4 | L | 12 | oval |
| -56.7 | -21.2 | L | 5 | oval |
| -56.6 | -16.2 | L | 5 | oval |
| -56.7 | -15.4 | L | 5 | oval |
| -56.7 | -16.3 | L | 5 | oval |
| -56.6 | -8.2 | L | 5-10 | oval |
| -56.7 | -8.1 | L | 5-10 | oval |
| -56.8 | -6.7 | L | 5-10 | oval |
| -56.6 | -7.8 | L | 5-10 | oval |
| -56.7 | -22.7 | L | 5 | negative |
| -56.6 | -20.1 | L | 6 | negative |
| -56.6 | -8.0 | L | 15-25 | oval |
| -56.7 | -6.0 | L | 15-25 | oval |
| -56.6 | -5.5 | L | 15-25 | oval |
| -56.6 | 16.8 | L | 25 | oval |
| -56.6 | 17.1 | L | 25 | oval |
| -56.7 | 16.9 | L | 20 | oval |
| -56.6 | 16.8 | L | 15 | oval |
| -56.8 | 17.0 | L | 25 | oval |
| -56.6 | 16.8 | L | 25 | oval |
| -56.6 | 16.9 | L | 22 | oval |
| -56.8 | 14.5 | L | 25 | oval |
| -56.6 | 14.0 | L | 15 | oval |
| -56.6 | 15.6 | L | 15 | oval |
| -56.6 | 14.7 | L | 15 | oval |
| -56.8 | 15.1 | L | 10 | oval |
| -56.7 | 14.8 | L | 12 | oval |
| -57.3 | 13.9 | L | 20 | oval |
| -57.0 | 18.2 | L | 25 | oval |
| -56.7 | 18.3 | L | 25 | oval |
| -57.0 | 18.2 | L | 15-20 | oval |
| -57.2 | 19.7 | L | 25 | oval |
| -57.2 | 20.4 | L | 30 | oval |
| -57.2 | 18.3 | L | 20 | oval |
| -56.6 | -9.2 | L | 15 | oval |
| -56.7 | -11.3 | L | 10 | oval |
| -56.6 | -10.0 | L | 15-20 | oval |
| -56.6 | -6.1 | L | 15-25 | oval |
| -56.6 | -9.8 | L | 15-25 | oval |

| Tm(°C) | Th(°C) | phase | size(μm) | shape |
|--------|--------|-------|----------|-------|
| -57.3 | 19.2 | L | 25 | irregular |
| -57.1 | 18.2 | L | 30 | irregular |
| -56.9 | 20.2 | L | 25 | irregular |
| -56.8 | 20.4 | L | 15 | irregular |
| -57.0 | 20.4 | L | 15 | irregular |
| -56.8 | 19.2 | L | 15-25 | irregular |
| -58.7 | 4.1 | L | 20-25 | tubular |
| -59.0 | 3.8 | L | 20-25 | tubular |
| -59.0 | 4.0 | L | 20-25 | tubular |
| -57.7 | 4.1 | L | 20-25 | tubular |
| -57.6 | 4.7 | l | 22 | tubular |
| -58.8 | 4.2 | L | 20-25 | tubular |
| -58.9 | 4.3 | L | 20-25 | tubular |
| -59.1 | 4.0 | L | 20-25 | tubular |
| -57.8 | 3.9 | L | 20-25 | tubular |
| -57.9 | 3.9 | L | 20-25 | tubular |
| -58.3 | 4.0 | L | 20-25 | tubular |
| -58.5 | 4.1 | L | 20-25 | tubular |
| -58.4 | 4.0 | L | 20-25 | tubular |
| -58.5 | 4.2 | L | 20-25 | tubular |
| -58.5 | -16.6 | L | 20-25 | tubular |
| -58.4 | -6.3 | L | 20-25 | tubular |
| -58.5 | -6.6 | L | 15 | oval |
| -58.6 | -6.5 | L | 10 | oval |
| -58.6 | -6.3 | L | 8 | oval |
| -58.5 | -3.2 | L | 5 | oval |
| -58.4 | -5.0 | L | 10 | oval |
| -58.4 | -2.5 | L | 15 | oval |
| -59.0 | -16.7 | L | 15 | oval |
| -58.8 | -13.5 | L | 15 | oval |
| -58.6 | -16.0 | L | 15 | oval |
| -58.6 | -17.3 | L | 5 | oval |
| -58.5 | -18.6 | L | 10 | oval |
| -58.9 | -25.4 | L | 3 | oval |
| -58.4 | -22.2 | L | 5 | oval |
| -58.5 | -16.9 | L | 5 | oval |
| -58.5 | -12.8 | L | 5-15 | oval |
| -58.5 | -25.4 | L | 5 | oval |
| -59.0 | -23.2 | L | 5 | oval |
| -58.8 | -18.6 | L | 15 | oval |
| -58.8 | -6.3 | L | 15 | oval |
| -58.8 | -6.2 | L | 10 | oval |
| -58.8 | -6.3 | L | 12 | oval |
| -58.8 | -6.4 | L | 8 | oval |

| Tm(°C) | Th(°C) | phase | size(μm) | shape |
|--------|--------|-------|----------|-------|
| -58.8 | -6.2 | L | 8 | oval |
| -58.9 | -25.4 | L | 5 | oval |
| -58.8 | -26.3 | L | 15 | oval |
| -58.4 | -25.3 | L | 12 | oval |
| -59.0 | -23.2 | L | 10 | oval |
| -57.7 | -25.4 | L | 8 | oval |
| -58.9 | -26.4 | L | 5-15 | oval |
| -58.4 | -25.8 | L | 10 | oval |
| -58.6 | -25.6 | L | 15 | oval |
| -58.4 | -25.5 | L | 15 | oval |
| -58.5 | -24.1 | L | 5 | oval |
| -58.8 | -26.6 | L | 15 | oval |
| -58.8 | -25.4 | L | 15 | oval |
| -56.6 | 12.8 | L | 10 | oval |
| -56.6 | -14.3 | L | <10 | neg |
| -56.6 | -7.9 | L | <10 | neg |
| -56.6 | -13.5 | L | <10 | neg |
| -56.6 | -13.4 | L | <10 | neg |
| -56.6 | -14.2 | L | <10 | neg |
| -56.6 | -13.5 | L | <10 | neg |
| -56.6 | 15.7 | L | 15-20 | irregular |
| -56.6 | 17.1 | L | 15-20 | irregular |
| -56.7 | 21.5 | L | 15-20 | irregular |
| -56.7 | -18.8 | L | <10 | neg |
| -56.6 | -16.2 | L | <10 | neg |
| -56.8 | 13.3 | L | <10 | neg |
| -56.6 | -8.6 | L | <10 | neg |
| -56.6 | -7.9 | L | <10 | neg |
| -56.6 | -8.5 | L | <10 | neg |
| -56.7 | -11.9 | L | <10 | neg |
| -56.8 | -8.7 | L | <10 | neg |
| -56.6 | -12.3 | L | <10 | neg |
| -56.6 | -8.8 | L | <10 | neg |
| -56.6 | -8.7 | L | <10 | neg |
| -56.6 | -11.1 | L | <10 | oval |

Nitrogen Fluid Inclusions

| Th (°C) | phase | size μm | occuerence | shape |
|---------|-------|---------|------------|-------|
| -146.9 | V | 14 | trails | irregular |
| -144.0 | V | 17 | trails | oval |
| -146.7 | V | 15 | trails | rectangular |
| -145.0 | V | 15 | trails | irrregular |
| -144.9 | V | 15 | trails | rectangular |
| -146.3 | V | 15 | trails | oval |
| -145.1 | V | 20 | trails | oval |
| -146.3 | V | 10 | trails | oval |
| -145.9 | V | 10 | trails | rectangular |
| -150.2 | V | 10 | trails | irregular |
| -147.2 | V | 15 | trails | irregular |
| -146.9 | V | 15 | trails | irregular |
| -146.6 | V | 15 | trails | irregular |
| -146.6 | V | 15 | trails | irregular |
| -146.7 | V | 10 | trails | irregular |
| -146.6 | V | 20 | trails | irregular |
| -146.8 | V | 25 | trails | irregular |
| -146.6 | V | 20 | trails | irregular |
| -146.6 | V | 20 | trails | irregular |
| -146.6 | V | 10 | trails | irregular |
| -145.7 | V | 15 | trails | irregular |
| -146.7 | V | 15 | trails | irregular |
| -146.9 | V | 20 | trails | irregular |
| -146.6 | V | 16 | trails | oval |
| -146.9 | V | 15 | trails | oval |
| -147.3 | V | 21 | trails | oval |
| -147.7 | V | 15 | trails | rectangular |
| -146.6 | V | 15 | trails | irregular |
| -141.4 | V | 30 | trails | rectangualr |
| -141.2 | V | 20 | trails | oval |
| -142.8 | V | 20 | trails | oval |
| -140.2 | V | 25 | trails | oval |
| -150.4 | V | 25 | trails | irregular |
| -150.6 | V | 10 | trails | oval |
| -147.6 | V | 15 | trails | irregular |
| -147.0 | V | 15 | trails | irregular |
| -146.5 | V | 26 | trails | oval |
| -146.4 | V | 15 | trails | irregular |
| -144.3 | V | 15 | trails | irregular |
| -147.0 | V | 10 | trails | oval |
| -146.5 | V | 10 | trails | oval |
| -147.1 | V | 27 | trails | oval |
| -163.0 | V | 16 | trails | oval |
| -146.2 | V | 15 | trails | oval |

Aqueous Fluid Inclusions

| Th (°C) | Tm (°C) | size (μm) | shape |
|---------|---------|-----------|-----------|
| 277.2 | -5.6 | 20 | oval |
| 265.3 | -5.2 | 15 | oval |
| 274.3 | -3.3 | 16 | oval |
| 270.0 | -4.2 | 19 | oval |
| 271.0 | -4.1 | 20 | oval |
| 269.0 | -5.1 | 15-20 | oval |
| 278.9 | -4.2 | 15-20 | oval |
| 275.4 | -4.3 | 15 | oval |
| 277.3 | -4.2 | 15 | oval |
| 277.4 | -3.2 | 15-20 | oval |
| 295.0 | -5.0 | 15-20 | oval |
| 297.7 | -8.4 | 15-20 | oval |
| 299.0 | -4.4 | 25-30 | irregular |
| 272.2 | -5.4 | 15-20 | oval |
| 292.3 | -5.4 | 35 | irregular |
| 298.7 | -4.4 | 20 | oval |
| 297.6 | -4.3 | 20 | oval |
| 305.4 | -3.4 | 15 | oval |
| 301.2 | -5.6 | 15-20 | oval |
| 299.8 | -4.5 | 15-20 | oval |
| 285.6 | -5.6 | 20 | oval |
| 310.7 | -5.8 | 25 | irregular |
| 301.4 | -4.6 | 15 | oval |
| 297.8 | -5.9 | 15 | oval |
| 269.6 | -5.3 | 15-20 | oval |
| 277.1 | -5.2 | 15-20 | oval |
| 276.7 | -3.2 | 15-20 | oval |
| 278.5 | -5.4 | 15-20 | oval |
| 265.4 | -5.6 | 15-20 | oval |
| 304.9 | -4.8 | 15 | oval |
| 292.3 | -4.9 | 21 | oval |
| 296.5 | -3.3 | 25 | oval |
| 295.8 | -4.2 | 15-20 | oval |
| 295.9 | -4.3 | 15 | oval |
| 297.6 | -4.3 | 15 | oval |
| 294.4 | -3.2 | 15-20 | oval |
| 305.0 | -4.5 | 15-20 | oval |
| 300.0 | -4.4 | 15-20 | oval |
| 297.0 | -4.6 | 20 | oval |
| 291.4 | -5.4 | 15-20 | oval |
| 297.0 | -3.2 | 25 | oval |

| T h (°C) | T m (°C) | size (μm) | shape |
|---|---|---|---|
| 332..8 | -5.4 | 15 | oval |
| 325.8 | -4.5 | 15-20 | oval |
| 332.6 | -4.4 | 15-20 | oval |
| 302.0 | -4.2 | 30 | irregular |
| 303.6 | -4.5 | 30 | irregular |
| 227.0 | -4.5 | 25 | oval |
| 232.4 | -4.6 | 15 | oval |
| 236.0 | -5.6 | 26 | oval |
| 235.6 | -4.3 | 24 | irregular |
| 233.6 | -5.6 | 18 | oval |
| 235.0 | -5.7 | 30 | irregular |
| 239.0 | -5.4 | 15-20 | oval |
| 241.5 | -5.8 | 26 | oval |
| 332.4 | -6.2 | 28 | oval |
| 317.9 | -6.1 | 15 | oval |
| 235.5 | -6.0 | 14 | oval |
| 308.7 | -5.7 | 10 | irregular |
| 336.4 | -5.6 | 8 | oval |
| 337.4 | -5.7 | 25 | oval |
| 336.5 | -4.3 | 10 | oval |
| 271.5 | -4.4 | 15-20 | oval |
| 263.0 | -4.7 | 22 | oval |
| 264.5 | -5.9 | 15 | oval |
| 276.4 | -5.6 | 15 | oval |
| 298.0 | -5.7 | 22 | oval |
| 291.0 | -5.6 | 25 | oval |
| 270.9 | -5.5 | 17 | oval |
| 236.7 | -5.8 | 16 | oval |
| 276.0 | -5.3 | 25 | oval |
| 280.0 | -4.8 | 120 | oval |
| 305.0 | -5.6 | 20 | oval |
| 276.8 | -5.6 | 20 | oval |
| 273.4 | -4.4 | 20 | oval |
| 232.1 | -4.9 | 25 | oval |
| 276.0 | -3.8 | 15 | oval |
| 261.0 | -5.1 | 15 | oval |
| 299.0 | -4.5 | 15 | oval |
| 268.0 | -4.6 | 15 | oval |
| 269.5 | -4.3 | 20 | oval |
| 260.1 | -5.7 | 20 | oval |
| 233.4 | -5.8 | 120 | oval |
| 278.0 | -4.6 | 20 | oval |
| 275.0 | -3.4 | 20 | oval |
| 275.6 | -4.7 | 20 | oval |
| 261.0 | -4.4 | 20 | oval |

| T h(°C) | T m (°C) | size (μm) | shape |
|---------|----------|-----------|-------|
| 277.3 | -4.6 | 20 | oval |
| 275.0 | -5.4 | 20 | oval |
| 275.6 | -5.3 | 20 | oval |
| 271.6 | -5.2 | 15 | oval |
| 268.5 | -5.7 | 15 | oval |
| 298.0 | -4.9 | 20 | oval |
| 293.0 | -4.7 | 15 | oval |
| 275.0 | -4.5 | 15-20 | oval |
| 290.5 | -2.5 | 15-20 | oval |
| 289.6 | -3.9 | 15-20 | oval |
| 299.0 | -2.8 | 15-20 | oval |
| 298.0 | -4.5 | 15-20 | oval |
| 255.6 | -4.4 | 15 | oval |
| 333.5 | -5.6 | 38 | irregular |
| 336.5 | -5.4 | 24 | oval |
| 334.4 | -5.7 | 24 | oval |
| 333.5 | -5 | 15 | oval |
| 332.1 | -5.4 | 15 | oval |
| 336.5 | -5.4 | 20 | oval |
| 335.6 | -4.2 | 10 | oval |
| 330.0 | -4.6 | 20 | oval |

# Appendix III Electron Microprobe Data

Garnet probe data, sample WN-7 mylonite.

| | | | | | | | |
|---|---|---|---|---|---|---|---|
| $SiO_2$ | 38.91 | 38.55 | 39.87 | 39.63 | 39.84 | 39.42 | 39.37 |
| $Al_2O_3$ | 23.76 | 26.05 | 21.18 | 22.26 | 22.53 | 22.31 | 22.15 |
| $TiO_2$ | 0.00 | 0.05 | 1.00 | 0.01 | 0.03 | 0.01 | 0.00 |
| $FeO$ | 31.94 | 32.38 | 32.08 | 31.29 | 31.04 | 30.35 | 30.91 |
| $MnO$ | 0.82 | 0.57 | 0.79 | 0.78 | 0.71 | 0.75 | 0.69 |
| $MgO$ | 5.41 | 5.52 | 5.95 | 6.53 | 6.57 | 6.68 | 6.74 |
| $Cr_2O_3$ | 0.00 | 0.00 | 0.00 | 0.00 | 0.00 | 0.00 | 0.00 |
| $CaO$ | 0.95 | 0.94 | 0.96 | 0.99 | 1.02 | 0.97 | 0.96 |
| $Na_2O$ | 0.00 | 0.00 | 0.00 | 0.00 | 0.00 | 0.00 | 0.00 |
| $K_2O$ | 0.00 | 0.00 | 0.00 | 0.00 | 0.00 | 0.00 | 0.00 |
| Total | 101.83 | 104.08 | 101.86 | 101.51 | 101.76 | 100.52 | 100.85 |
| | | | | | | | |
| cat Si | 5.97 | 5.78 | 6.13 | 6.08 | 6.09 | 6.09 | 6.07 |
| cat Al | 4.29 | 4.60 | 3.83 | 4.02 | 4.05 | 4.06 | 4.03 |
| cat Ti | 0.00 | 0.00 | 0.11 | 0.00 | 0.00 | 0.00 | 0.00 |
| cat Fe | 4.10 | 4.06 | 4.12 | 4.01 | 3.96 | 3.92 | 3.99 |
| cat Mn | 0.10 | 0.07 | 0.10 | 0.10 | 0.09 | 0.09 | 0.09 |
| cat Mg | 1.23 | 1.23 | 1.36 | 1.49 | 1.49 | 1.54 | 1.55 |
| cat Cr | 0.00 | 0.00 | 0.00 | 0.00 | 0.00 | 0.00 | 0.00 |
| cat Ca | 0.15 | 0.15 | 0.15 | 0.16 | 0.16 | 0.16 | 0.16 |
| cat Na | 0.00 | 0.00 | 0.00 | 0.00 | 0.00 | 0.00 | 0.00 |
| cat K | 0.00 | 0.00 | 0.00 | 0.00 | 0.00 | 0.00 | 0.00 |
| Total cations | 15.87 | 15.91 | 15.83 | 15.89 | 15.87 | 15.87 | 15.90 |
| | | | | | | | |
| Almandine | 0.73 | 0.73 | 0.71 | 0.69 | 0.69 | 0.68 | 0.68 |
| Grossular | 0.02 | 0.02 | 0.02 | 0.02 | 0.02 | 0.02 | 0.02 |
| Pyrope | 0.22 | 0.22 | 0.23 | 0.25 | 0.26 | 0.26 | 0.26 |
| Spessartine | 0.01 | 0.01 | 0.01 | 0.01 | 0.01 | 0.01 | 0.01 |
| Fe/(Fe+Mg) | 0.76 | 0.76 | 0.75 | 0.72 | 0.72 | 0.71 | 0.72 |

| 39.39 | 39.47 | 37.38 | 39.51 | 39.31 | 38.53 | 37.16 | 31.79 |
|---|---|---|---|---|---|---|---|
| 22.13 | 22.54 | 26.83 | 22.31 | 22.51 | 25.13 | 30.49 | 26.02 |
| 0.00 | 0.00 | 0.02 | 0.02 | 0.00 | 0.05 | 0.08 | 0.02 |
| 31.16 | 30.80 | 27.66 | 30.16 | 29.93 | 27.29 | 17.74 | 24.38 |
| 0.90 | 0.80 | 0.65 | 0.90 | 0.84 | 0.79 | 0.50 | 0.62 |
| 6.84 | 6.96 | 6.12 | 6.98 | 7.02 | 6.39 | 4.56 | 5.11 |
| 0.00 | 0.00 | 0.00 | 0.00 | 0.00 | 0.00 | 0.00 | 0.00 |
| 0.98 | 1.03 | 1.05 | 0.93 | 1.00 | 1.13 | 3.67 | 3.21 |
| 0.00 | 0.00 | 0.00 | 0.00 | 0.00 | 0.00 | 0.00 | 0.00 |
| 0.00 | 0.00 | 0.00 | 0.00 | 0.00 | 0.00 | 0.00 | 0.00 |
| 101.43 | 101.63 | 99.73 | 100.83 | 100.64 | 99.3 | 94.21 | 91.18 |
| 6.06 | 6.04 | 5.74 | 6.08 | 6.05 | 5.93 | 5.77 | 5.38 |
| 4.01 | 4.06 | 4.86 | 4.04 | 4.09 | 4.56 | 5.58 | 5.19 |
| 0.00 | 0.00 | 0.00 | 0.00 | 0.00 | 0.00 | 0.01 | 0.00 |
| 4.00 | 3.94 | 3.55 | 3.88 | 3.85 | 3.51 | 2.30 | 3.45 |
| 0.11 | 0.10 | 0.08 | 0.11 | 0.11 | 0.10 | 0.06 | 0.09 |
| 1.57 | 1.58 | 1.40 | 1.60 | 1.61 | 1.46 | 1.05 | 1.29 |
| 0.00 | 0.00 | 0.00 | 0.00 | 0.00 | 0.00 | 0.00 | 0.00 |
| 0.16 | 0.17 | 0.17 | 0.15 | 0.16 | 0.18 | 0.61 | 0.58 |
| 0.00 | 0.00 | 0.00 | 0.00 | 0.00 | 0.00 | 0.00 | 0.00 |
| 0.00 | 0.00 | 0.00 | 0.00 | 0.00 | 0.00 | 0.00 | 0.00 |
| 15.93 | 15.92 | 15.82 | 15.89 | 15.89 | 15.77 | 15.41 | 16.01 |
| 0.68 | 0.67 | 0.68 | 0.67 | 0.67 | 0.66 | 0.57 | 0.63 |
| 0.02 | 0.02 | 0.03 | 0.02 | 0.03 | 0.03 | 0.15 | 0.10 |
| 0.26 | 0.27 | 0.26 | 0.27 | 0.28 | 0.27 | 0.26 | 0.23 |
| 0.02 | 0.01 | 0.01 | 0.02 | 0.01 | 0.02 | 0.01 | 0.01 |
| 0.71 | 0.71 | 0.71 | 0.70 | 0.70 | 0.70 | 0.68 | 0.72 |

| | | | | | |
|---|---|---|---|---|---|
| 38.67 | 38.87 | 39.39 | 39.07 | 39.65 | 39.86 |
| 22.48 | 22.47 | 22.48 | 22.52 | 22.27 | 22.15 |
| 0.00 | 0.00 | 0.02 | 0.02 | 0.00 | 0.00 |
| 29.38 | 29.34 | 29.76 | 29.76 | 30.17 | 30.04 |
| 0.77 | 0.78 | 0.87 | 0.83 | 0.81 | 0.67 |
| 6.97 | 7.16 | 7.05 | 6.97 | 7.07 | 6.95 |
| 0.00 | 0.00 | 0.00 | 0.00 | 0.00 | 0.00 |
| 1.22 | 1.13 | 1.05 | 0.93 | 0.93 | 0.87 |
| 0.00 | 0.00 | 0.00 | 0.00 | 0.00 | 0.00 |
| 0.00 | 0.00 | 0.00 | 0.00 | 0.00 | 0.00 |
| 99.52 | 99.78 | 100.64 | 100.12 | 100.89 | 100.57 |
| | | | | | |
| 6.02 | 6.03 | 6.06 | 6.05 | 6.09 | 6.11 |
| 4.12 | 4.11 | 4.08 | 4.11 | 4.03 | 4.01 |
| 0.00 | 0.00 | 0.00 | 0.00 | 0.00 | 0.00 |
| 3.82 | 3.81 | 3.83 | 3.85 | 3.87 | 3.86 |
| 0.10 | 0.10 | 0.11 | 0.11 | 0.10 | 0.08 |
| 1.61 | 1.65 | 1.61 | 1.61 | 1.62 | 1.59 |
| 0.00 | 0.00 | 0.00 | 0.00 | 0.00 | 0.00 |
| 0.20 | 0.18 | 0.17 | 0.15 | 0.15 | 0.14 |
| 0.00 | 0.00 | 0.00 | 0.00 | 0.00 | 0.00 |
| 0.00 | 0.00 | 0.00 | 0.00 | 0.00 | 0.00 |
| 15.90 | 15.90 | 15.89 | 15.89 | 15.88 | 15.85 |
| | | | | | |
| 0.66 | 0.66 | 0.66 | 0.67 | 0.67 | 0.67 |
| 0.03 | 0.03 | 0.03 | 0.02 | 0.02 | 0.02 |
| 0.28 | 0.28 | 0.28 | 0.28 | 0.28 | 0.28 |
| 0.01 | 0.01 | 0.02 | 0.01 | 0.01 | 0.01 |
| 0.70 | 0.69 | 0.70 | 0.70 | 0.70 | 0.70 |

| | | | | | | | |
|---|---|---|---|---|---|---|---|
| 36.40 | 36.26 | 36.43 | 36.88 | 36.58 | 36.71 | 36.38 | 36.48 |
| 22.85 | 22.85 | 23.23 | 23.29 | 23.96 | 23.05 | 23.03 | 22.92 |
| 0.05 | 0.05 | 0.01 | 0.00 | 0.00 | 0.02 | 0.06 | 0.07 |
| 33.34 | 33.7 | 32.86 | 33.39 | 33.66 | 33.58 | 33.07 | 32.82 |
| 1.18 | 1.224 | 1.17 | 1.22 | 1.21 | 1.12 | 1.26 | 1.18 |
| 6.57 | 6.69 | 6.61 | 6.63 | 6.58 | 6.55 | 6.42 | 6.47 |
| 0.00 | 0.00 | 0.00 | 0.00 | 0.00 | 0.00 | 0.00 | 0.00 |
| 1.25 | 1.2 | 1.30 | 1.29 | 1.34 | 1.20 | 1.28 | 1.23 |
| 0.00 | 0.00 | 0.00 | 0.00 | 0.00 | 0.00 | 0.00 | 0.00 |
| 0.00 | 0.00 | 0.00 | 0.00 | 0.00 | 0.00 | 0.00 | 0.00 |
| 101.67 | 102.04 | 101.63 | 102.72 | 103.36 | 102.28 | 101.54 | 101.20 |

| | | | | | | | |
|---|---|---|---|---|---|---|---|
| 5.69 | 5.66 | 5.68 | 5.70 | 5.62 | 5.70 | 5.69 | 5.72 |
| 4.21 | 4.21 | 4.27 | 4.24 | 4.3 | 4.22 | 4.25 | 4.23 |
| 0.00 | 0.00 | 0.0 | 0.00 | 0.00 | 0.00 | 0.00 | 0.00 |
| 4.36 | 4.41 | 4.29 | 4.31 | 4.33 | 4.36 | 4.33 | 4.30 |
| 0.15 | 0.162 | 0.15 | 0.16 | 0.15 | 0.14 | 0.16 | 0.15 |
| 1.53 | 1.5 | 1.54 | 1.52 | 1.51 | 1.52 | 1.50 | 1.51 |
| 0.00 | 0.000 | 0.0 | 0.00 | 0.00 | 0.00 | 0.00 | 0.00 |
| 0.21 | 0.2 | 0.21 | 0.21 | 0.22 | 0.20 | 0.21 | 0.20 |
| 0.00 | 0.00 | 0.0 | 0.00 | 0.00 | 0.00 | 0.00 | 0.00 |
| 0.00 | 0.00 | 0.00 | 0.00 | 0.00 | 0.00 | 0.00 | 0.00 |
| 16.18 | 16.22 | 16.17 | 16.17 | 16.19 | 16.17 | 16.17 | 16.15 |

| | | | | | | | |
|---|---|---|---|---|---|---|---|
| 0.69 | 0.69 | 0.69 | 0.69 | 0.69 | 0.70 | 0.69 | 0.69 |
| 0.03 | 0.03 | 0.03 | 0.03 | 0.03 | 0.03 | 0.03 | 0.03 |
| 0.24 | 0.24 | 0.24 | 0.24 | 0.24 | 0.24 | 0.24 | 0.24 |
| 0.02 | 0.02 | 0.02 | 0.02 | 0.02 | 0.02 | 0.02 | 0.02 |
| 0.74 | 0.73 | 0.73 | 0.73 | 0.74 | 0.74 | 0.74 | 0.74 |

| | | | | | | | |
|---|---|---|---|---|---|---|---|
| 36.41 | 36.61 | 36.48 | 36.41 | 36.62 | 36.48 | 36.41 | 36.62 |
| 23.01 | 22.94 | 22.92 | 23.10 | 22.94 | 22.92 | 23.01 | 22.94 |
| 0.00 | 0.00 | 0.07 | 0.00 | 0.00 | 0.00 | 0.00 | 0.00 |
| 33.42 | 33.19 | 32.82 | 33.42 | 33.19 | 33.82 | 33.42 | 33.19 |
| 1.11 | 1.26 | 1.18 | 1.11 | 1.26 | 1.189 | 1.11 | 1.26 |
| 6.68 | 6.65 | 6.46 | 6.68 | 6.65 | 6.649 | 6.62 | 6.65 |
| 0.00 | 0.00 | 0.00 | 0.00 | 0.00 | 0.00 | 0.00 | 0.00 |
| 1.27 | 1.21 | 1.23 | 1.27 | 1.21 | 1.23 | 1.27 | 1.21 |
| 0.00 | 0.00 | 0.00 | 0.00 | 0.00 | 0.000 | 0.00 | 0.00 |
| 0.00 | 0.00 | 0.00 | 0.00 | 0.00 | 0.000 | 0.00 | 0.00 |
| 101.91 | 101.89 | 101.20 | 102.00 | 101.89 | 102.308 | 101.85 | 101.89 |
| 5.68 | 5.71 | 5.72 | 5.67 | 5.71 | 5.685 | 5.68 | 5.71 |
| 4.23 | 4.21 | 4.23 | 4.24 | 4.21 | 4.210 | 4.23 | 4.21 |
| 0.00 | 0.00 | 0.00 | 0.00 | 0.00 | 0.00 | 0.00 | 0.00 |
| 4.36 | 4.33 | 4.30 | 4.36 | 4.33 | 4.408 | 4.36 | 4.33 |
| 0.14 | 0.16 | 0.15 | 0.14 | 0.16 | 0.15 | 0.14 | 0.16 |
| 1.55 | 1.54 | 1.51 | 1.55 | 1.54 | 1.54 | 1.54 | 1.54 |
| 0.00 | 0.00 | 0.00 | 0.00 | 0.00 | 0.000 | 0.00 | 0.00 |
| 0.21 | 0.20 | 0.20 | 0.21 | 0.20 | 0.20 | 0.21 | 0.20 |
| 0.00 | 0.00 | 0.00 | 0.00 | 0.00 | 0.00 | 0.00 | 0.00 |
| 0.00 | 0.00 | 0.00 | 0.00 | 0.00 | 0.00 | 0.00 | 0.00 |
| 16.19 | 16.17 | 16.15 | 16.19 | 16.17 | 16.21 | 16.19 | 16.17 |
| 0.69 | 0.69 | 0.69 | 0.69 | 0.69 | 0.69 | 0.69 | 0.69 |
| 0.03 | 0.03 | 0.03 | 0.03 | 0.03 | 0.03 | 0.03 | 0.03 |
| 0.24 | 0.24 | 0.24 | 0.24 | 0.24 | 0.24 | 0.24 | 0.24 |
| 0.02 | 0.02 | 0.02 | 0.02 | 0.02 | 0.02 | 0.02 | 0.02 |
| 0.73 | 0.73 | 0.74 | 0.73 | 0.73 | 0.74 | 0.73 | 0.73 |

| | | | | | | | |
|---|---|---|---|---|---|---|---|
| 36.64 | 36.64 | 36.87 | 36.59 | 36.80 | 36.77 | 37.09 | 36.90 |
| 22.58 | 22.90 | 22.72 | 22.92 | 23.09 | 23.35 | 22.98 | 22.17 |
| 0.00 | 0.00 | 0.00 | 0.02 | 0.06 | 0.01 | 0.01 | 0.01 |
| 33.29 | 33.62 | 33.41 | 33.88 | 33.11 | 33.18 | 33.47 | 33.38 |
| 1.17 | 1.11 | 1.19 | 1.03 | 1.11 | 1.17 | 1.25 | 1.09 |
| 6.56 | 6.66 | 6.59 | 6.66 | 6.53 | 6.61 | 6.60 | 6.55 |
| 0.00 | 0.00 | 0.00 | 0.00 | 0.00 | 0.00 | 0.00 | 0.00 |
| 1.29 | 1.33 | 1.12 | 1.23 | 1.32 | 1.39 | 1.27 | 0.10 |
| 0.00 | 0.00 | 0.00 | 0.00 | 0.00 | 0.00 | 0.00 | 0.00 |
| 0.00 | 0.00 | 0.00 | 0.00 | 0.00 | 0.00 | 0.00 | 0.00 |
| 101.55 | 102.29 | 101.94 | 102.36 | 102.12 | 102.49 | 102.70 | 100.22 |
| | | | | | | | |
| 5.74 | 5.70 | 5.74 | 5.69 | 5.72 | 5.69 | 5.73 | 5.83 |
| 4.16 | 4.20 | 4.17 | 4.20 | 4.23 | 4.26 | 4.19 | 4.13 |
| 0.00 | 0.00 | 0.00 | 0.00 | 0.00 | 0.00 | 0.00 | 0.00 |
| 4.36 | 4.37 | 4.35 | 4.41 | 4.30 | 4.29 | 4.33 | 4.41 |
| 0.15 | 0.14 | 0.15 | 0.13 | 0.15 | 0.15 | 0.16 | 0.14 |
| 1.53 | 1.54 | 1.53 | 1.54 | 1.51 | 1.52 | 1.52 | 1.54 |
| 0.00 | 0.00 | 0.00 | 0.00 | 0.00 | 0.00 | 0.00 | 0.00 |
| 0.21 | 0.22 | 0.18 | 0.20 | 0.22 | 0.23 | 0.21 | 0.01 |
| 0.00 | 0.00 | 0.00 | 0.00 | 0.00 | 0.00 | 0.00 | 0.00 |
| 0.00 | 0.00 | 0.00 | 0.00 | 0.00 | 0.00 | 0.00 | 0.00 |
| 16.17 | 16.19 | 16.16 | 16.20 | 16.15 | 16.17 | 16.16 | 16.09 |
| | | | | | | | |
| 0.69 | 0.69 | 0.69 | 0.70 | 0.69 | 0.69 | 0.69 | 0.72 |
| 0.00 | 0.03 | 0.03 | 0.03 | 0.03 | 0.03 | 0.03 | 0.00 |
| 0.24 | 0.24 | 0.24 | 0.24 | 0.24 | 0.24 | 0.24 | 0.25 |
| 0.02 | 0.02 | 0.02 | 0.02 | 0.02 | 0.02 | 0.02 | 0.02 |
| 0.74 | 0.73 | 0.74 | 0.74 | 0.74 | 0.73 | 0.74 | 0.74 |

| | | | | | | | |
|---|---|---|---|---|---|---|---|
| 36.97 | 36.98 | 37.15 | 37.16 | 37.33 | 37.35 | 36.98 | 37.05 |
| 22.13 | 22.76 | 23.09 | 22.91 | 23.33 | 23.17 | 23.04 | 22.96 |
| 0.07 | 0.00 | 0.07 | 0.01 | 0.04 | 0.00 | 0.00 | 0.04 |
| 33.38 | 33.62 | 33.73 | 32.86 | 33.60 | 34.43 | 33.79 | 34.02 |
| 1.09 | 1.02 | 1.09 | 1.16 | 1.15 | 1.12 | 1.13 | 1.09 |
| 6.55 | 6.61 | 6.47 | 6.62 | 6.27 | 6.54 | 6.23 | 6.70 |
| 0.00 | 0.00 | 0.00 | 0.00 | 0.00 | 0.00 | 0.00 | 0.00 |
| 0.00 | 0.00 | 0.00 | 0.00 | 0.00 | 0.00 | 0.00 | 0.00 |
| 1.36 | 1.25 | 1.31 | 1.11 | 1.28 | 1.29 | 1.20 | 1.30 |
| 0.00 | 0.00 | 0.00 | 0.00 | 0.00 | 0.00 | 0.00 | 0.00 |
| 0.00 | 0.00 | 0.00 | 0.00 | 0.00 | 0.00 | 0.00 | 0.00 |
| 101.58 | 102.26 | 102.93 | 101.84 | 102.77 | 103.91 | 102.38 | 103.19 |
| 5.79 | 5.74 | 5.73 | 5.77 | 5.73 | 5.72 | 5.74 | 5.71 |
| 4.08 | 4.17 | 4.20 | 4.19 | 4.25 | 4.18 | 4.22 | 4.17 |
| 0.00 | 0.00 | 0.00 | 0.00 | 0.00 | 0.00 | 0.00 | 0.00 |
| 4.37 | 4.37 | 4.35 | 4.27 | 4.34 | 4.41 | 4.39 | 4.39 |
| 0.14 | 0.13 | 0.14 | 0.15 | 0.15 | 0.14 | 0.15 | 0.14 |
| 1.53 | 1.53 | 1.49 | 1.53 | 1.45 | 1.49 | 1.43 | 1.54 |
| 0.00 | 0.00 | 0.00 | 0.00 | 0.00 | 0.00 | 0.00 | 0.00 |
| 0.22 | 0.20 | 0.21 | 0.18 | 0.21 | 0.21 | 0.20 | 0.21 |
| 0.00 | 0.00 | 0.00 | 0.00 | 0.00 | 0.00 | 0.00 | 0.00 |
| 0.00 | 0.00 | 0.00 | 0.00 | 0.00 | 0.00 | 0.00 | 0.00 |
| 16.15 | 16.16 | 16.15 | 16.12 | 16.13 | 16.18 | 16.14 | 16.19 |
| 0.69 | 0.70 | 0.70 | 0.69 | 0.71 | 0.70 | 0.71 | 0.69 |
| 0.03 | 0.03 | 0.03 | 0.03 | 0.03 | 0.03 | 0.03 | 0.03 |
| 0.24 | 0.24 | 0.24 | 0.25 | 0.23 | 0.23 | 0.23 | 0.24 |
| 0.02 | 0.02 | 0.02 | 0.02 | 0.02 | 0.02 | 0.02 | 0.02 |
| 0.74 | 0.74 | 0.74 | 0.73 | 0.75 | 0.74 | 0.75 | 0.74 |

| | | | |
|---|---|---|---|
| 37.46 | 37.48 | | |
| 22.97 | 22.94 | | |
| 0.03 | 0.00 | | |
| 33.13 | 34.6 | | |
| 1.06 | 1.50 | | |
| 6.89 | 6.01 | | |
| 0.00 | 0.00 | | |
| 1.24 | 1.24 | | |
| 0.00 | 0.00 | | |
| 0.00 | 0.00 | | |
| 102.80 | 103.85 | | |
| | | | |
| 5.77 | 5.76 | | |
| 4.17 | 4.15 | | |
| 0.00 | 0.00 | | |
| 4.26 | 4.45 | | |
| 0.13 | 0.19 | | |
| 1.58 | 1.37 | | |
| 0.00 | 0.00 | | |
| 0.20 | 0.20 | | |
| 0.00 | 0.00 | | |
| 0.00 | 0.00 | | |
| 16.14 | 16.15 | | |
| | | | |
| 0.68 | 0.71 | | |
| 0.03 | 0.03 | | |
| 0.25 | 0.22 | | |
| 0.02 | 0.03 | | |
| 0.72 | 0.76 | | |

Cordierite probe data, sample WN-7 mylonite.

| | | | | | | | |
|---|---|---|---|---|---|---|---|
| SiO$_2$ | 48.31 | 47.89 | 47.28 | 43.66 | 94.70 | 47.71 | 49.03 |
| Al$_2$O$_3$ | 32.57 | 32.64 | 32.23 | 21.29 | 0.08 | 33.01 | 31.73 |
| TiO$_2$ | 0.00 | 0.00 | 0.00 | 0.00 | 0.00 | 0.00 | 0.00 |
| FeO | 5.77 | 5.58 | 5.54 | 28.59 | 0.04 | 5.62 | 5.58 |
| MnO | 0.14 | 0.08 | 0.11 | 1.04 | 0.00 | 0.06 | 0.11 |
| MgO | 9.84 | 9.73 | 9.61 | 4.38 | 0.02 | 9.52 | 9.42 |
| Cr$_2$O$_3$ | 0.00 | 0.00 | 0.00 | 0.00 | 0.00 | 0.00 | 0.00 |
| CaO | 0.00 | 0.00 | 0.00 | 0.00 | 0.00 | 0.00 | 0.00 |
| Na$_2$O | 0.07 | 0.09 | 0.13 | 0.00 | 0.00 | 0.09 | 0.12 |
| K$_2$O | 0.00 | 0.00 | 0.00 | 0.00 | 0.00 | 0.00 | 0.00 |
| Total | 96.72 | 96.03 | 94.92 | 98.98 | 94.85 | 96.03 | 96.01 |
| | | | | | | | |
| cat Si | 5.00 | 4.98 | 4.98 | 5.02 | 8.99 | 4.96 | 5.09 |
| cat Al | 3.97 | 4.00 | 4.00 | 2.89 | 0.00 | 4.05 | 3.88 |
| cat Ti | 0.00 | 0.00 | 0.00 | 0.00 | 0.00 | 0.00 | 0.00 |
| cat Fe | 0.50 | 0.48 | 0.48 | 2.75 | 0.00 | 0.49 | 0.48 |
| cat Mn | 0.01 | 0.00 | 0.01 | 0.10 | 0.00 | 0.00 | 0.01 |
| cat Mg | 1.51 | 1.51 | 1.51 | 0.75 | 0.00 | 1.47 | 1.46 |
| cat Cr | 0.00 | 0.00 | 0.00 | 0.00 | 0.00 | 0.00 | 0.00 |
| cat Ca | 0.00 | 0.00 | 0.00 | 0.00 | 0.00 | 0.00 | 0.00 |
| cat Na | 0.01 | 0.02 | 0.02 | 0.00 | 0.00 | 0.01 | 0.02 |
| cat K | 0.00 | 0.00 | 0.00 | 0.00 | 0.00 | 0.00 | 0.00 |
| Total cations | 11.01 | 11.01 | 11.02 | 11.52 | 9.00 | 11.01 | 10.97 |
| | | | | | | | |
| Fe/(Fe+Mg) | 0.24 | 0.24 | 0.24 | 0.78 | 0.53 | 0.24 | 0.24 |

| 92.69 | 34.79 | 46.02 | 47.46 | 47.98 | 47.90 | 48.01 | 48.05 |
|---|---|---|---|---|---|---|---|
| 1.87 | 21.93 | 31.25 | 32.51 | 32.38 | 32.49 | 32.45 | 32.59 |
| 0.00 | 0.00 | 0.00 | 0.00 | 0.00 | 0.00 | 0.00 | 0.00 |
| 2.04 | 3.23 | 5.30 | 5.86 | 5.72 | 5.75 | 5.53 | 5.90 |
| 0.07 | 0.07 | 0.12 | 0.08 | 0.08 | 0.16 | 0.09 | 0.06 |
| 0.35 | 6.34 | 9.63 | 9.81 | 9.80 | 9.81 | 9.66 | 9.71 |
| 0.00 | 0.00 | 0.00 | 0.00 | 0.00 | 0.00 | 0.00 | 0.00 |
| 0.00 | 0.00 | 0.00 | 0.00 | 0.00 | 0.00 | 0.00 | 0.00 |
| 0.04 | 1.00 | 0.11 | 0.10 | 0.05 | 0.07 | 0.06 | 0.00 |
| 0.00 | 0.00 | 0.00 | 0.00 | 0.00 | 0.00 | 0.00 | 0.00 |
| 97.07 | 67.40 | 92.46 | 95.84 | 96.03 | 96.20 | 32.51 | 96.34 |
| 8.73 | 5.15 | 4.98 | 4.96 | 5.00 | 4.98 | 0.01 | 4.99 |
| 0.20 | 3.82 | 3.98 | 4.00 | 3.97 | 3.98 | 11.97 | 3.99 |
| 0.00 | 0.00 | 0.00 | 0.00 | 0.00 | 0.00 | 0.00 | 0.00 |
| 0.16 | 0.40 | 0.48 | 0.51 | 0.49 | 0.50 | 0.00 | 0.51 |
| 0.00 | 0.01 | 0.01 | 0.00 | 0.00 | 0.01 | 0.00 | 0.00 |
| 0.05 | 1.40 | 1.55 | 1.53 | 1.52 | 1.52 | 0.00 | 1.50 |
| 0.00 | 0.00 | 0.00 | 0.00 | 0.00 | 0.00 | 0.00 | 0.00 |
| 0.00 | 0.00 | 0.00 | 0.00 | 0.00 | 0.00 | 0.00 | 0.00 |
| 0.00 | 0.28 | 0.02 | 0.02 | 0.01 | 0.01 | 0.00 | 0.00 |
| 0.00 | 0.00 | 0.00 | 0.00 | 0.00 | 0.00 | 0.00 | 0.00 |
| 9.16 | 11.07 | 11.03 | 11.04 | 11.01 | 11.02 | 11.99 | 11.01 |
| 0.76 | 0.22 | 0.23 | 0.25 | 0.24 | 0.24 | 0.24 | 0.25 |

| | | | | | | | |
|---|---|---|---|---|---|---|---|
| 47.10 | 48.11 | 48.29 | 47.36 | 47.59 | 48.18 | 47.56 | 48.75 |
| 34.73 | 32.85 | 32.68 | 32.36 | 32.22 | 32.37 | 32.32 | 32.34 |
| 0.00 | 0.00 | 0.00 | 0.00 | 0.00 | 0.00 | 0.00 | 0.00 |
| 5.55 | 5.71 | 5.76 | 5.77 | 5.746 | 5.68 | 5.78 | 5.65 |
| 0.10 | 0.08 | 0.06 | 0.10 | 0.13 | 0.06 | 0.05 | 0.12 |
| 9.08 | 9.57 | 9.72 | 9.78 | 9.82 | 9.76 | 9.91 | 9.83 |
| 0.00 | 0.00 | 0.00 | 0.00 | 0.00 | 0.00 | 0.00 | 0.00 |
| 0.00 | 0.00 | 0.00 | 0.00 | 0.00 | 0.00 | 0.00 | 0.00 |
| 0.06 | 0.08 | 0.08 | 0.06 | 0.02 | 0.05 | 0.09 | 0.06 |
| 0.00 | 0.00 | 0.00 | 0.00 | 0.00 | 0.00 | 0.00 | 0.00 |
| 96.63 | 96.42 | 96.60 | 95.46 | 95.53 | 96.12 | 95.73 | 96.77 |
| 4.87 | 4.99 | 5.00 | 4.97 | 4.98 | 5.01 | 4.97 | 5.03 |
| 4.23 | 4.01 | 3.98 | 4.00 | 3.98 | 3.96 | 3.98 | 3.93 |
| 0.00 | 0.00 | 0.00 | 0.00 | 0.00 | 0.00 | 0.00 | 0.00 |
| 0.48 | 0.49 | 0.49 | 0.50 | 0.50 | 0.49 | 0.50 | 0.48 |
| 0.00 | 0.00 | 0.00 | 0.00 | 0.01 | 0.00 | 0.00 | 0.01 |
| 1.40 | 1.48 | 1.50 | 1.53 | 1.53 | 1.51 | 1.54 | 1.51 |
| 0.00 | 0.00 | 0.00 | 0.00 | 0.00 | 0.00 | 0.00 | 0.00 |
| 0.00 | 0.00 | 0.00 | 0.00 | 0.00 | 0.00 | 0.00 | 0.00 |
| 0.01 | 0.01 | 0.01 | 0.01 | 0.00 | 0.01 | 0.01 | 0.01 |
| 0.00 | 0.00 | 0.00 | 0.00 | 0.00 | 0.00 | 0.00 | 0.00 |
| 11.01 | 11.00 | 11.01 | 11.03 | 11.02 | 11.00 | 11.03 | 11.00 |
| 0.25 | 0.25 | 0.25 | 0.25 | 0.25 | 0.25 | 0.25 | 0.24 |

82

Cordierite probe data, sample WN-7 host rock

| | | | | | | | |
|---|---|---|---|---|---|---|---|
| SiO$_2$ | 46.51 | 49.53 | 48.69 | 48.11 | 48.08 | 48.24 | 47.97 |
| Al$_2$O$_3$ | 33.84 | 33.40 | 32.74 | 32.41 | 32.52 | 32.74 | 32.67 |
| TiO$_2$ | 0.00 | 0.00 | 0.00 | 0.00 | 0.00 | 0.00 | 0.00 |
| FeO | 2.84 | 5.52 | 6.44 | 6.17 | 6.31 | 6.32 | 6.22 |
| MnO | 0.05 | 0.02 | 1.00 | 0.03 | 0.09 | 0.08 | 0.07 |
| MgO | 2.56 | 7.48 | 9.84 | 9.69 | 9.57 | 9.69 | 9.46 |
| Cr$_2$O$_3$ | 0.00 | 0.00 | 0.00 | 0.00 | 0.00 | 0.00 | 0.00 |
| CaO | 0.00 | 0.00 | 0.00 | 0.00 | 0.00 | 0.00 | 0.00 |
| Na$_2$O | 0.26 | 0.22 | 0.12 | 0.11 | 0.13 | 0.08 | 0.12 |
| K$_2$O | 0.00 | 0.00 | 0.00 | 0.00 | 0.00 | 0.00 | 0.00 |
| Total | 86.01 | 96.19 | 98.84 | 96.55 | 96.72 | 97.16 | 96.53 |
| | | | | | | | |
| cat Si | 5.25 | 5.12 | 4.97 | 4.99 | 4.99 | 4.98 | 4.98 |
| cat Al | 4.50 | 4.07 | 3.94 | 3.96 | 3.97 | 3.98 | 4.00 |
| cat Ti | 0.00 | 0.00 | 0.00 | 0.00 | 0.00 | 0.00 | 0.00 |
| cat Fe | 0.26 | 0.47 | 0.55 | 0.53 | 0.54 | 0.54 | 0.54 |
| cat Mn | 0.00 | 0.00 | 0.08 | 0.00 | 0.00 | 0.00 | 0.00 |
| cat Mg | 0.43 | 1.15 | 1.49 | 1.50 | 1.48 | 1.49 | 1.46 |
| cat Cr | 0.00 | 0.00 | 0.00 | 0.00 | 0.00 | 0.00 | 0.00 |
| cat Ca | 0.00 | 0.00 | 0.00 | 0.00 | 0.00 | 0.00 | 0.00 |
| cat Na | 0.05 | 0.04 | 0.02 | 0.02 | 0.02 | 0.01 | 0.02 |
| cat K | 0.00 | 0.00 | 0.00 | 0.00 | 0.00 | 0.00 | 0.00 |
| Total cations | 10.52 | 10.86 | 11.07 | 11.03 | 11.03 | 11.03 | 11.02 |
| | | | | | | | |
| Fe/(Fe+Mg) | 0.38 | 0.29 | 0.26 | 0.26 | 0.27 | 0.26 | 0.26 |

| 48.74 | 47.96 | 47.41 | 47.30 | 48.68 | 48.03 | 47.44 | 48.15 |
|---|---|---|---|---|---|---|---|
| 32.32 | 32.53 | 32.20 | 32.17 | 32.63 | 32.70 | 33.55 | 32.49 |
| 0.00 | 0.00 | 0.00 | 0.00 | 0.00 | 0.00 | 0.00 | 0.00 |
| 6.02 | 6.32 | 6.38 | 6.19 | 6.10 | 6.46 | 6.15 | 6.18 |
| 0.09 | 0.12 | 0.06 | 0.07 | 0.09 | 0.09 | 0.10 | 0.04 |
| 9.49 | 9.62 | 9.53 | 9.53 | 9.54 | 9.27 | 6.41 | 9.50 |
| 0.00 | 0.00 | 0.00 | 0.00 | 0.00 | 0.00 | 0.00 | 0.00 |
| 0.00 | 0.00 | 0.00 | 0.00 | 0.00 | 0.00 | 0.00 | 0.00 |
| 0.12 | 0.15 | 0.16 | 0.11 | 0.11 | 0.13 | 0.18 | 0.11 |
| 0.00 | 0.00 | 0.00 | 0.00 | 0.00 | 0.00 | 0.00 | 0.00 |
| 96.80 | 96.72 | 95.77 | 95.42 | 97.17 | 96.71 | 93.85 | 96.51 |
| 5.04 | 4.98 | 4.97 | 4.97 | 5.02 | 4.98 | 5.04 | 5.00 |
| 3.94 | 3.98 | 3.98 | 3.99 | 3.96 | 4.00 | 4.20 | 3.97 |
| 0.00 | 0.00 | 0.00 | 0.00 | 0.00 | 0.00 | 0.00 | 0.00 |
| 0.52 | 0.54 | 0.56 | 0.54 | 0.52 | 0.56 | 0.54 | 0.53 |
| 0.00 | 0.01 | 0.00 | 0.00 | 0.00 | 0.00 | 0.00 | 0.00 |
| 1.46 | 1.49 | 1.49 | 1.49 | 1.46 | 1.43 | 1.01 | 1.47 |
| 0.00 | 0.00 | 0.00 | 0.00 | 0.00 | 0.00 | 0.00 | 0.00 |
| 0.00 | 0.00 | 0.00 | 0.00 | 0.00 | 0.00 | 0.00 | 0.00 |
| 0.02 | 0.03 | 0.03 | 0.02 | 0.02 | 0.02 | 0.03 | 0.02 |
| 0.00 | 0.00 | 0.00 | 0.00 | 0.00 | 0.00 | 0.00 | 0.00 |
| 11.00 | 11.04 | 11.04 | 11.04 | 11.00 | 11.02 | 10.86 | 11.02 |
| 0.26 | 0.26 | 0.27 | 0.26 | 0.26 | 0.28 | 0.35 | 0.26 |

| | | | | | |
|---|---|---|---|---|---|
| 47.15 | 47.49 | 47.43 | 47.49 | 47.48 | 47.42 |
| 32.46 | 32.19 | 32.18 | 32.21 | 32.36 | 32.22 |
| 0.00 | 0.00 | 0.00 | 0.00 | 0.00 | 0.00 |
| 6.12 | 6.12 | 6.41 | 5.90 | 6.11 | 5.98 |
| 0.06 | 0.06 | 0.04 | 0.12 | 0.09 | 0.08 |
| 9.54 | 9.66 | 9.58 | 9.46 | 9.48 | 9.58 |
| 0.00 | 0.00 | 0.00 | 0.00 | 0.00 | 0.00 |
| 0.00 | 0.00 | 0.00 | 0.00 | 0.00 | 0.00 |
| 0.08 | 0.10 | 0.11 | 0.10 | 0.15 | 0.10 |
| 0.00 | 0.00 | 0.00 | 0.00 | 0.00 | 0.00 |
| 95.44 | 95.63 | 95.77 | 95.29 | 95.69 | 95.39 |
| 4.95 | 4.98 | 4.97 | 4.99 | 4.97 | 4.98 |
| 4.02 | 3.98 | 3.97 | 3.99 | 3.99 | 3.99 |
| 0.00 | 0.00 | 0.00 | 0.00 | 0.00 | 0.00 |
| 0.53 | 0.53 | 0.56 | 0.51 | 0.53 | 0.52 |
| 0.00 | 0.00 | 0.00 | 0.01 | 0.00 | 0.00 |
| 1.49 | 1.51 | 1.49 | 1.48 | 1.48 | 1.50 |
| 0.00 | 0.00 | 0.00 | 0.00 | 0.00 | 0.00 |
| 0.00 | 0.00 | 0.00 | 0.00 | 0.00 | 0.00 |
| 0.01 | 0.02 | 0.02 | 0.02 | 0.03 | 0.02 |
| 0.00 | 0.00 | 0.00 | 0.00 | 0.00 | 0.00 |
| 11.03 | 11.03 | 11.04 | 11.02 | 11.03 | 11.03 |
| 0.26 | 0.26 | 0.27 | 0.25 | 0.26 | 0.25 |

Biotite probe data, sample WN-

|  |  |  |  |  |  |  |  |  |
|---|---|---|---|---|---|---|---|---|
| $SiO_2$ | 36.10 | 36.73 | 34.78 | 35.92 | 31.21 | 35.93 | 37.09 | 37.16 |
| $TiO_2$ | 2.69 | 2.68 | 2.41 | 2.69 | 0.78 | 1.12 | 2.28 | 2.29 |
| $Al_2O_3$ | 20.56 | 19.46 | 22.21 | 20.09 | 29.96 | 21.85 | 17.99 | 20.79 |
| $Cr_2O_3$ | 0.00 | 0.00 | 0.00 | 0.08 | 0.06 | 0.04 | 0.24 | 0.14 |
| MgO | 13.54 | 13.40 | 12.42 | 12.82 | 12.78 | 16.11 | 15.50 | 14.84 |
| CaO | 0.02 | 0.00 | 0.05 | 0.07 | 0.55 | 0.13 | 0.00 | 0.10 |
| MnO | 0.09 | 0.00 | 0.07 | 0.04 | 0.07 | 0.00 | 0.01 | 0.12 |
| FeO | 14.93 | 15.19 | 13.96 | 14.61 | 11.20 | 11.42 | 14.11 | 13.10 |
| BaO | 0.00 | 0.00 | 0.00 | 0.00 | 0.00 | 0.00 | 0.00 | 0.00 |
| $Na2O$ | 0.11 | 0.14 | 0.10 | 0.07 | 0.29 | 0.08 | 0.08 | 0.30 |
| $K_2O$ | 9.26 | 8.91 | 8.77 | 9.26 | 7.59 | 8.96 | 9.37 | 8.09 |
| $H_2O$ | 3.95 | 3.84 | 3.81 | 3.82 | 3.83 | 3.94 | 3.83 | 3.74 |
| F | 0.35 | 0.53 | 0.49 | 0.50 | 0.57 | 0.41 | 0.58 | 0.94 |
| total | 101.56 | 100.70 | 98.94 | 99.81 | 98.66 | 100.17 | 100.88 | 101.25 |
|  |  |  |  |  |  |  |  |  |
| cat Si | 5.24 | 5.31 | 5.15 | 5.30 | 4.55 | 5.20 | 5.41 | 5.32 |
| cat Ti | 0.29 | 0.29 | 0.26 | 0.29 | 0.08 | 0.12 | 0.25 | 0.24 |
| cat Al | 3.51 | 3.35 | 3.88 | 3.49 | 5.15 | 3.72 | 3.09 | 3.51 |
| cat Cr | 0.00 | 0.00 | 0.00 | 0.00 | 0.00 | 0.00 | 0.02 | 0.01 |
| cat Mg | 2.93 | 2.92 | 2.74 | 2.82 | 2.77 | 3.47 | 3.37 | 3.17 |
| cat Ca | 0.00 | 0.00 | 0.00 | 0.01 | 0.08 | 0.02 | 0.00 | 0.01 |
| cat Mn | 0.01 | 0.00 | 0.00 | 0.00 | 0.00 | 0.00 | 0.00 | 0.01 |
| cat Fe | 1.81 | 1.81 | 1.72 | 1.80 | 1.36 | 1.41 | 1.72 | 1.57 |
| cat Ba | 0.00 | 0.00 | 0.00 | 0.00 | 0.00 | 0.00 |  | 0.00 |
| cat Na | 0.03 | 0.03 | 0.03 | 0.02 | 0.08 | 0.02 | 0.02 | 0.08 |
| cat K | 7.69 | 1.66 | 1.65 | 1.74 | 1.41 | 1.65 | 1.79 | 1.49 |
| Total Cations | 15.57 | 15.50 | 15.48 | 15.52 | 15.53 | 15.65 | 15.65 | 15.44 |
|  |  |  |  |  |  |  |  |  |
| Fe/(Fe +Mg) | 0.38 | 0.39 | 0.39 | 0.39 | 0.33 | 0.29 | 0.34 | 0.33 |